KINEMATICALLY COMPLETE STUDIES OF COLLISIONS BETWEEN SIMPLE MOLECULAR IONS AND NEUTRAL GAS TARGETS

by

NORA GERLINE JOHNSON

B. A., Augustana College, 2005

A THESIS

submitted in partial fulfillment of the
requirements for the degree

MASTER OF SCIENCE

Department of Physics
College of Arts and Sciences

KANSAS STATE UNIVERSITY
Manhattan, Kansas
2010

Approved by:

Major Professor
Itzik Ben-Itzhak

Copyright

Abstract

Collisions between simple diatomic molecular ions and target atoms have previously been limited to studying a subset of reaction channels for a given experiment, or, for cases where all reaction channels involved were measured, only the cross sections have been reported in literature. Experimentalists are faced with the challenge of improving their techniques for studying these collisions in order to gain further physical insight into the processes which occur. Our group has made progress in studying the molecular dissociation channels from the collisions via a coincidence three-dimensional momentum imaging technique. This technique allows us to measure all reaction channels involved simultaneously, while separating the channels from each other. By re-design of the experimental apparatus, i.e. changing the target from a gas cell to an open geometry jet, we have gained the ability to measure recoil ions produced in the collision in addition to the molecular fragments. Furthermore, we can also study collisions where the molecular projectile does not dissociate as long as it scatters to large angles. Results from the collision cell setup will be shown and discussed as well as first results from the jet setup. This work is a contribution to a larger project, and the emphasis for this stage will be placed on the development of the experimental technique as well as improvements for the future of the project.

Table of Contents

List of Figures

List of Tables

Acknowledgments

As I look back over the course of my life, there are so many people that have influenced me in so many ways, and I would like to thank them all. First and foremost, I would like to thank Dr. Eric Wells, who sparked my interest in AMO physics. I would like to acknowledge my great advisor, Dr. Itzik Ben-Itzhak, as well as Dr. Kevin Carnes for their support in building a new collision apparatus and taking measurements with it. Also, the members of the Ben-Itzhak group, whom I have had the great experience of working with and learning from – it would be impossible to be in the position to write a thesis without you. This includes the talented post-docs Dr. Pengquian Wang and Dr. Jarlath McKenna, the graduate students: Max Sayler, Bishwanath Gaire, and Mohammad Zohrabi, and the undergraduate students: Mat Leonard and Eli Parke, and Ben Berry. In particular, I would like to acknowledge Ben Berry, who helped with simulations and conducting the experiments and our visiting professor, Dr. Wania Wolff, who did much of the analysis of the non-dissociative channels. I would also like to acknowledge Dag Hathiramani and Jack Maseberg for their prior contributions to the project.

Also, helpful in making it both through graduate level courses and everyday life, I would like to note my appreciation for Dyan and Sean McBride, Fran Mateycik, Jackie and Mike Chini, Adrian Carmichael, and Mohammad Zohrabi. From my time at Augustana College, I would like to thank Bethany Amundson, Stacia Wagner and Kelli Gross. In addition, I would like to recognize the REU students whose enthusiasm was infectious: Sam Fahrenholtz, Leah Van Nahmen, David Miller, and Forrest Roberts.

On the technical side of things, many thanks to Mike Wells, Al Rankin, Scott Chainey, and Charles Fehrenbach, especially for aligning the 'EBIS-C' beamline, solving any mechanical or electrical problems that ever came about, and teaching me how to run the ion source.

Lastly, I would like to thank my family and Matthias Kling for their support.

Dedication

I would like to dedicate this thesis to Matthias Kling, for it is with him in mind that I have written every word.

Chapter 1

Introduction

The progress of experimental research and technology are tightly knit. In general, along with a novel tool comes a novel experimental result. The focus of this thesis will be the innovative use of existing tools to gain physical insight into slow collision processes between molecular ions and atoms. We choose to study such collision systems as they have well known Coulomb interactions, and we can learn much about the dynamics of the processes involved.

In general atomic collision physics is well understood [1] compared to molecular collisions with atoms. Molecule-atom collisions are much more complex, since the vibrational and rotational degrees of freedom are active, not to mention that molecules have more intricate electronic structure. Collisional processes between simple diatomic molecules and atoms have been of interest in astronomy, injection heating of plasmas, aeronomy, laser modeling, and simple chemical reactions for decades [2, 3, and references therein]. Collisions between diatomic molecular ions and noble gas atoms are rich with physical phenomena, as seen in the variety of reaction channels which result from a few keV simple diatomic molecular ion, AB^+, impinging on an atomic target, X. In this study AB^+ is typically H_2^+, HD^+ or HeH^+ and X is a noble gas target such as argon.

$$AB^+ + X \rightarrow A + B^+ + X \text{ or } A^+ + B + X, \qquad \textbf{CID} \qquad (1.1)$$

$$\rightarrow A + B + X^+, \qquad \textbf{DC} \qquad (1.2)$$

$$\rightarrow A^+ + B^+ + X + e^-, \qquad \textbf{EL} \qquad (1.3)$$

$$\rightarrow AB + X^+, \qquad \textbf{NDC} \qquad (1.4)$$

$$\rightarrow AB^+ + X^+ + e^-, \qquad \textbf{NDTI} \qquad (1.5)$$

$$\rightarrow A^+ + B + X^+ + e^- \text{ or } A + B^+ + X^+ + e^-, \qquad \textbf{CID-TI} \qquad (1.6)$$

$$\rightarrow A^+ + B^+ + X^+ + 2e^-. \qquad \textbf{EL-TI} \qquad (1.7)$$

Explicitly, the acronyms for each channel are: collision induced dissociation (CID), dissociative capture (DC), electron loss (EL), non-dissociative capture (NDC), non-dissociative target ionization (NDTI), collision induced dissociation accompanied by target ionization (CID-TI), and simultaneous projectile and target ionization (EL-TI).

A main focus of previous experimental work from the 1960's and 1970's was on the dominant channels: CID (channel 1.1) and DC (channel 1.2) [4–11]. The experimental methods during these two decades commonly employed post-interaction deflectors (electrostatic or magnetic) to separate the different charged species in position (e.g. see ref. [12]). Such an experimental method was reliable for measuring the scattering angles and energy distribution of the various fragments. The drawback was that the measurements were not in coincidence. Hence, for CID, usually only the ionic fragment was measured (e.g. see references [8–10]).

As DC's products are both neutral, it is easier to separate them from the ion beam, and therefore DC was normally the less complicated channel to measure. For this reason, DC is the better studied process. Even prior to 1965, when McClure [10] determined the angular distribution of the fast H fragments from 5-80 keV H_2^+ incident on H_2, there was general interest in the DC process [13–15].

Beginning in the 1980's a coincidence technique was developed for the capture channel.

The first coincidence DC studies were accomplished by de Bruijn *et al.*, who collided few keV H_2^+ with gas phase Ar, H_2, Mg, Na, and Cs targets [16]. Subsequently, coincidence experiments were performed by Wu *et al.* [17], Saito *et al.* [18], Schmidt *et al.* [19], and Posthumus *et al.* [20]. These works are elaborated on in chapter 3.

Coincidence CID measurements for H_2^+ were performed, for example, by Meierjohann and Vogler in the 1970's [11], by Suzuki *et al.* in the 1980's [21] and by McGrath *et al.* more recently [22]. However, only total cross sections or fractional yield analysis has been accomplished for these studies. Brenot *et al.* [23] and Fayeton *et al.* [24] have studied the coincidence CID process for Na_2^+ incident on He at keV energies and extracted valuable physical information including kinetic energy release (KER) and scattering angle of the center of mass. In doing so, they separated the various contributing mechanisms of the CID process for the sodium dimer - He system and gained an understanding of the reaction dynamics.

The H_2^+ experiments mentioned above did indeed first reveal the complexities of CID. In particular, there appeared to be two contributions in the angular distribution, one peaking at $\theta = 90°$ and the other at 0° and 180° (for the definition of θ, see Fig. 1.1), see Ref. [5]. Many explanations for the two contributions were offered, but the only one which proved true was first postulated by Vogler and Seibt [25]. They proposed that the feature at 90° was due to dissociation caused by vibrational excitation while the feature peaked at 0° and 180° was due to the expected electronic transition $1s\sigma_g \rightarrow 2p\sigma_u$.

Green and Peek developed a theory for the electronic CID process based on the Born approximation [26] in which they treated only the electronic process (see chapter 4 for more details). In a publication a year later, Green attempted to develop a theory for the vibrationally excited dissociation mechanism using the classical-impulse binary collision model [27]. However, he only obtained qualitative understanding of the process as a result of convoluting the vibrational and electronic contributions together. Green managed, however, to solidify Vogler and Seibt's suggestion that the contribution aligned perpendicular to

the collision velocity was due to a vibrational excitation mechanism. Nevertheless, it was necessary to further develop experimental techniques so that the CID mechanisms could be separated for H_2^+ collisions.

Beyond channels 1.1 and 1.2 for keV molecular ions with atomic targets, Suzuki *et al.* identified many of the other competing channels using post-interaction deflectors to separate the differently charged products. By detecting both projectiles and recoil ions, they compared the reaction cross sections for channels 1.1 - 1.5 [21]. Suzuki *et al.'s* studies spanned the 4-16 keV energy range for H_2^+ ion beams on He, Ne and Ar.

McGrath *et al.* have measured the cross-sections for all channels, 1.1 - 1.7, for 20-100 keV H_2^+ incident on H atoms [22]. They observe a moderate energy dependence of these cross-sections. Furthermore, Hennecart and Pascale performed classical trajectory Monte Carlo simulations to provide a theory basis for McGrath *et al.'s* measurements. For most channels, the agreement was found to be good [28].

Our group has implemented a coincidence 3D molecular imaging experimental technique to further study the reaction channels mentioned above. There are multiple stages of development on this project leading to the ultimate goal of achieving vibrational resolution for the molecular breakup. The first stage of development was largely undertaken by previous members of Prof. Ben-Itzhak's research group. These initial steps were to develop a setup with which we image the molecular dissociation. I joined the project during the data analysis of this first step, to which I contributed significantly, and therefore will include the results in this thesis.

In the previous measurements, we used a "cell" setup (see chapter 2 for experimental details) to study the molecular breakup of CID, channel 1.1, and DC, channel 1.2. Both channels are measured simultaneously and are well separated from each other in time. Observables include transverse momentum transfer to the center of mass, KER, scattering angle, orientation (ϕ) and molecular alignment(θ). The axial recoil approximation is enforced for θ (considering the channels where the projectile breaks), and the velocity of the

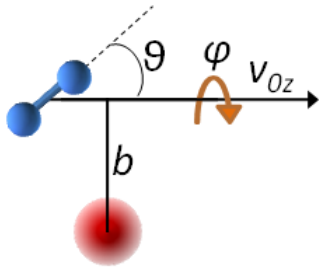

Figure 1.1: Schematic of the molecular ion – atom collision system, where v_{0z} is the velocity of the ion beam at the point of interaction, b is the impact parameter, θ is the angle between the axis of molecular dissociation and the beam velocity and ϕ is the azimuthal angle.

ion beam at the point of interaction is taken to be the average value. Fig. 1.1 outlines these relevant collision parameters. For CID, one goal was to study the vibrational and electronic processes individually. We were successful in this goal, and have devised a simplistic model for describing angular dependence for the two processes. Further studies with HeH^+ projectiles will also be highlighted. The processes that comprise CID for H_2^+ and HeH^+ are well resolved in these measurements and are further discussed in chapter 4. Likewise, the processes which comprise the DC channel are discussed in detail in chapter 3.

Having made progress on the detailed analysis of the "cell" setup data, we can form hypotheses based on what we learned from the molecular dissociation for what we might observe if we also measure the recoil ions. For example, we learned from the previous measurements that the vibrational CID process occurs for very close collisions. For such cases, it seems likely that the target might also ionize. By measuring recoiling ions in coincidence with this channel, i.e. channel 1.6, we can answer this question and therefore better understand this process.

The second stage of this project, which I was leading, was to develop an experimental system for simultaneous measurement of molecular dissociation and recoil ion imaging. In addition to what we originally sought to measure, we also discovered that we can measure

large-momentum-transfer molecules which coincide with recoiling ions, i.e. channels 1.4 and 1.5.

In our most recent measurements (with the "jet" setup, see chapter 2 for experimental details) for 3 keV H_2^+ on argon we distinctly observe channels 1.1, 1.2, and 1.4 - 1.6. Channel 1.3 is expected to be a small contribution at this low energy and will, for homonuclear molecules, appear as background to the more dominant DC channel, since both channels will appear at the same time difference. Also, we do not observe channel 1.7 at the collision energies which we have studied so far.

The main strength of the "jet" setup is that we can measure the complete kinematics for the channels where neither a neutral recoil nor an electron is produced (namely channels 1.2 and 1.4). We can also measure reaction channels for which the projectile does not dissociate if the transverse momentum transfer between the projectile and the target is large enough for the molecule to escape the Faraday cup. Another strength for the "jet" setup is that all reaction channels are measured simultaneously and therefore comparison amongst all channels can be made under the same experimental conditions.

Of particular interest to this study are: (1) the transverse momentum, which is approximately inversely related to the impact parameter of the collision, (2) kinetic energy release (KER) and (3) the angular dependence, for the reaction channels where the projectile fragments, and (4) the reaction Q values, for the reaction channels where a recoil ion is produced. Unfortunately, the Q values have proven to be difficult quantities to measure with the current resolution and calibration methods. So, I will instead point out the experimental parameters that need to be improved in order to determine the Q values better.

The focus of this thesis is to present a method for achieving the goals outlined above. Therefore, the bulk of the thesis is presented in chapter two, which describes the experimental apparatuses as well as the coincidence imaging techniques employed, allowing us to simultaneously measure all reaction channels on a single detector. Chapter three discusses DC. The focus of chapter four is CID. The separation of the mechanisms that comprise this

channel is discussed in detail. Also, a comparison is made between H_2^+ and HeH^+ under similar conditions, resulting in drastically different outcomes, which will be described. Chapter five outlines the progress which has been made in understanding the non-dissociative processes, NDC and NDTI. Chapter six gives an overview of the results and draws a comparison among the different reaction channels involved. Finally, chapter seven provides conclusions as well as future directions in which this experimental method can be extended.

Chapter 2

Experimental Methods

Few keV collisions between the most fundamental molecules, H_2^+, HD^+ and HeH^+, and noble gas atoms were studied with an initial goal of separating the various mechanisms involved. Of particular interest are electronic and vibrational excitation mechanisms leading to dissociation, since Green [27] performed calculations to fit previous experiments [5]. The two mechanisms were not cleanly separated in the earlier measurements, and so theories which tried to account for both cases were convoluted and therefore inconclusive. The experimental setup and techniques that allow for such separation are discussed in this chapter. In addition, a second goal (after the first was realized) of measuring recoiling ions in coincidence was set. The experimental apparatus for achieving this goal is discussed in section 2.2.

2.1 Experimental Setup: Target Cell Method

Few keV H_2^+, HD^+ and HeH^+ molecular ion beams were generated through electron impact ionization in an ion source, explicitly,

$$AB + e^- \rightarrow AB^+ + 2e^-. \tag{2.1}$$

A Penning ion gauge source – operating at low pressures – was utilized for producing H_2^+ and HD^+ beams, while a cold cathode direct current type source – operating at high pressures – was used in production of a HeH^+ beam.

After generation in the ion source, the molecular ion beam follows the path depicted in Fig. 2.1. The analyzing magnet selectively allows the ions with the correct momentum to charge ratio to pass though. Einzel lenses and four-jaw slits are used to focus and collimate the beam. An electrostatic steerer helps to direct the beam into the interaction region.

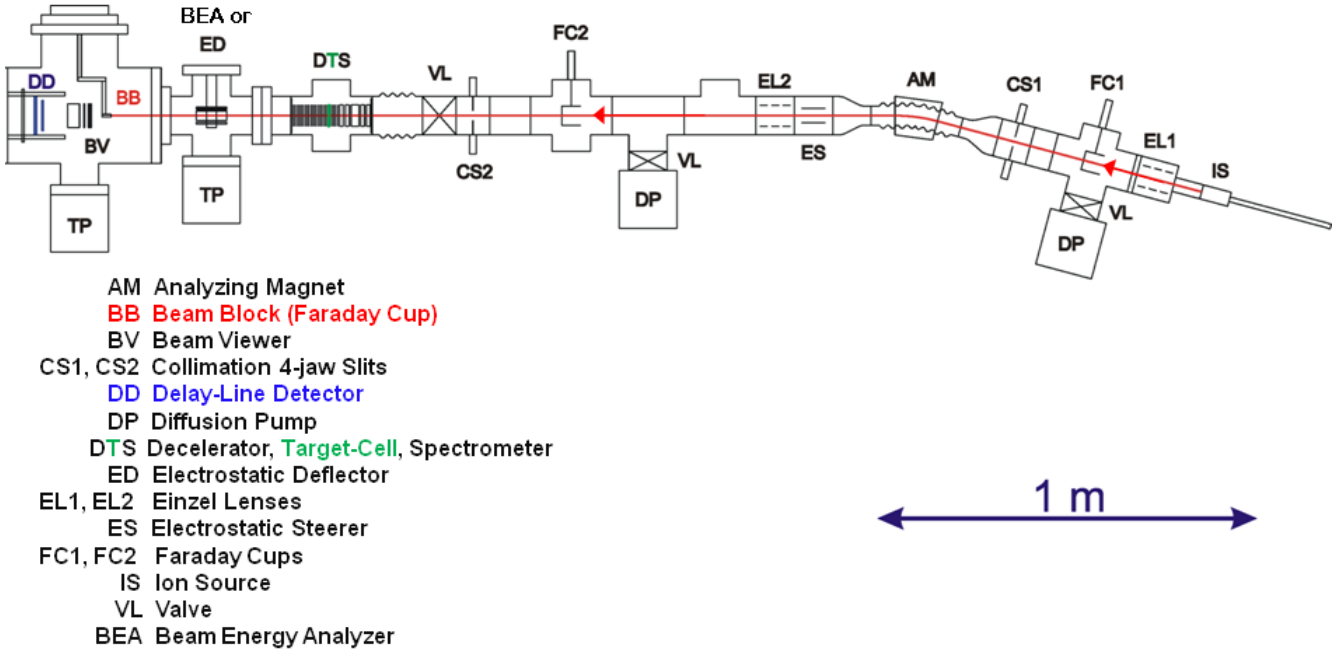

Figure 2.1: Schematic of the beamline using a gas target cell.

The interaction region is preceded by an electrostatic decelerator which slows the beam to the desired collision energy. The interaction region itself is within a thin (2 mm long) target cell. Typically, the target cell is filled to a pressure of about 0.4 mTorr with argon or helium gas. The entrance of the cell is 0.5 mm in diameter – defining the largest ion beam diameter and also reducing the amount of scattered beam that reaches the detector – and the exit aperture is 0.95 mm. The exit aperture allows scattering up to 45° and therefore is not a source of losses in the experiment.

On the exit side of the target cell is a longitudinal spectrometer, as shown in Fig. 2.2. The spectrometer is comprised of 18 rings, connected though a resistor chain, creating a

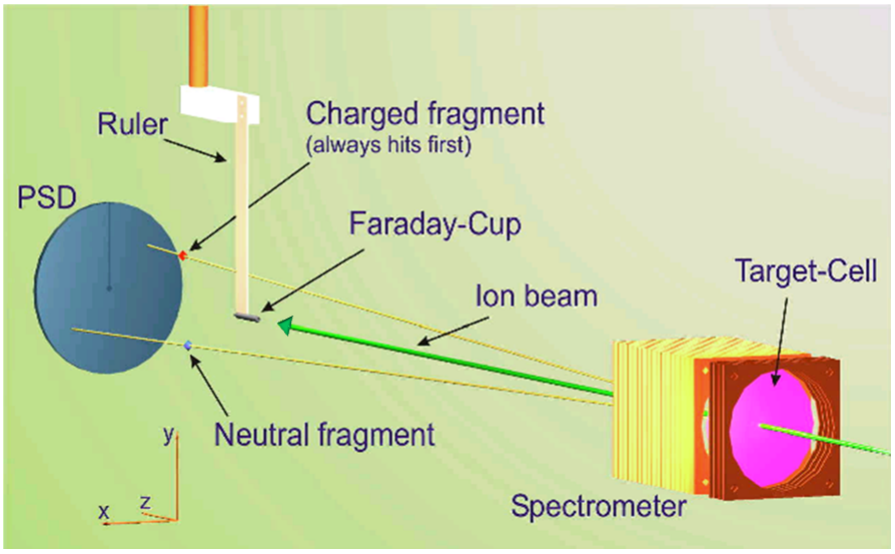

Figure 2.2: Schematic of the cell setup from the interaction to the detector. The spectrometer provides a longitudinal field which accelerates the charged fragments. The primary ion beam is blocked by a small Faraday cup. Fragments are imaged on a time and position sensitive detector (PSD). Note that the ruler is referred to as a bar in the text.

cylindrically symmetric electric field which falls off uniformly along its axis (except for edge effects). The purpose of the spectrometer is to accelerate the charged beam fragments and therefore make it possible for us to distinguish between ionic and neutral fragments – thus providing a means to separate the different channels.

The primary ion beam is blocked by a 2 mm diameter Faraday cup approximately 170 mm in front of the detector serving two purposes: (1) protecting the detector by blocking the ion beam and (2) providing a current measurement for normalization purposes.

The detector is time and position sensitive, consisting of 80 mm diameter microchannel plates in a chevron configuration and a delay line anode. The timing signals generated by both ion and neutral fragment impact are picked from the front of the microchannel plate.

The advantages of such a setup are: (1) DC and CID can be measured simultaneously (2) beam current can be very low (on the order of hunderds of femtoamperes) due to the relatively high target density in the cell, which is good for keeping the scattered beam rate on the detector low (3) tuning the beam through the target is easier (see more details in

section 2.2).

There is one main disadvantage of this experimental technique, which is that the recoil ions cannot be measured because there is no extraction field across the cell. Without the information from the recoil ion, the experiment is kinematically *in*complete for the DC channel. Therefore, a second experimental setup was developed. The main difference between the two setups is that the gas cell is replaced by a jet. The open geometry of the jet setup then allows us to measure the recoil ions in addition to the beam fragments.

2.2 Experimental Setup: Supersonic Jet Method

The molecular ion beam for the "jet" setup was also generated in an electron impact ion source[1]. Fig. 2.3 shows a schematic of the beamline components. The beam is mass selected by an analyzing magnet. Two sets of Einzel lenses and three sets of four-jaw slits are used to focus and collimate the beam. The slits for this setup are also used for reducing the scattering rate of the beam on the detector[2]. The beam is directed to the interaction region by X and Y electrostatic steerers.

Similar to the gas cell setup, the beam is decelerated to the desired collision energy prior to the interaction region. A schematic of the "jet" setup from the decelerator to the detector is shown in Fig. 2.4. The fifth ring with the small (2 mm diameter) aperture separates the deceleration and acceleration regions. Counting from the grounded ring of the decelerator, the supersonic jet flows upward between the sixth and seventh spectrometer rings. The supersonic jet was previously built for a different set of measurements and a description can be found in Ref. [29]. The open geometry of the jet allows for detection of recoil ions.

[1]The ion source used here is a Microtech model EX05, capable of producing beams in the 0.1 to 5 keV energy range. By floating the platform on which the source is located, energy beams up to 10 keV are currently possible.

[2]In the "cell" setup, the entrance to the target cell did an adequate job of reducing the beam scatter, therefore fewer slits were needed.

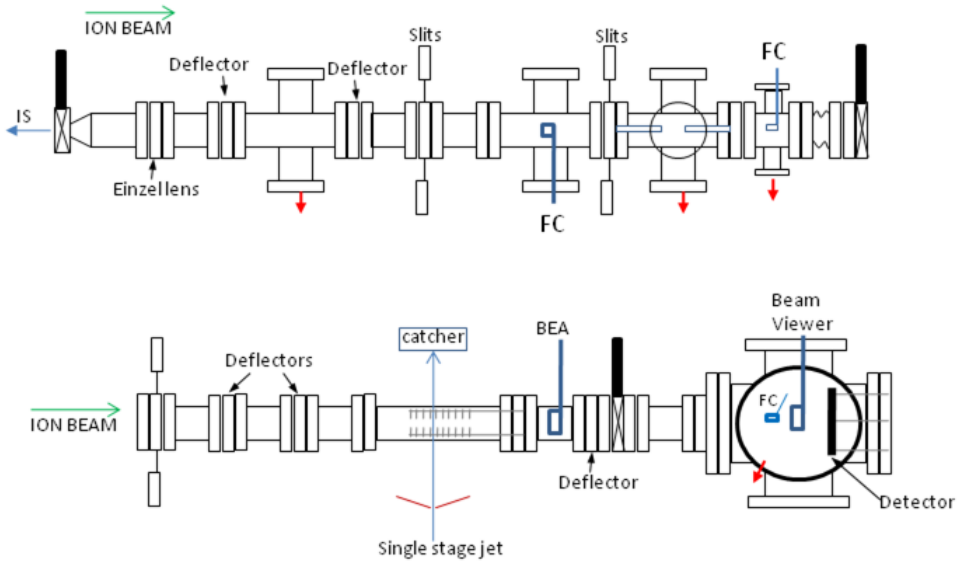

Figure 2.3: Schematic drawing (not to scale) of the jet beamline. Note that the beam viewer is used for tuning purposes and details can be found in Sayler's Ph.D. thesis [30]. Acronyms are beam-energy analyzer (BEA) and Faraday cup (FC).

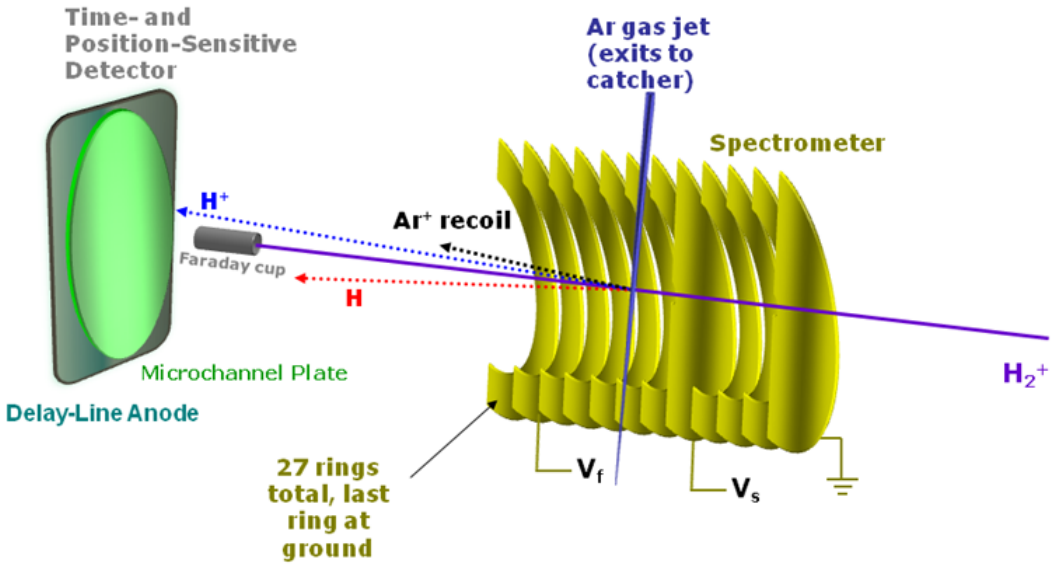

Figure 2.4: Schematic of the jet setup from the interaction to the detector. The advantage of the open-geometry jet is the capability of detecting recoil ions produced in the interaction, otherwise the imaging concept is the same as for the cell setup.

Table 2.1: Definitions of variables for Fig. 2.5. As the virtual spectrometer is still under development for the jet setup, only the real dimension of the spectrometer are given here.

	variable	virtual	real	description
Cell	l_0	5.6 mm	5.9 mm	first field-free region
	l_1	95.2 mm	95.1 mm	extraction field
	l_2	660.0 mm	659.8 mm	drift region
	l	l_0+l_1+l_2	l_0+l_1+l_2	total distance
Jet	l_1		27.1 mm	first extraction field
	l_2		96.3 mm	second extraction field
	l_3		679.2 mm	drift region
	l		l_1+l_2+l_3	total distance

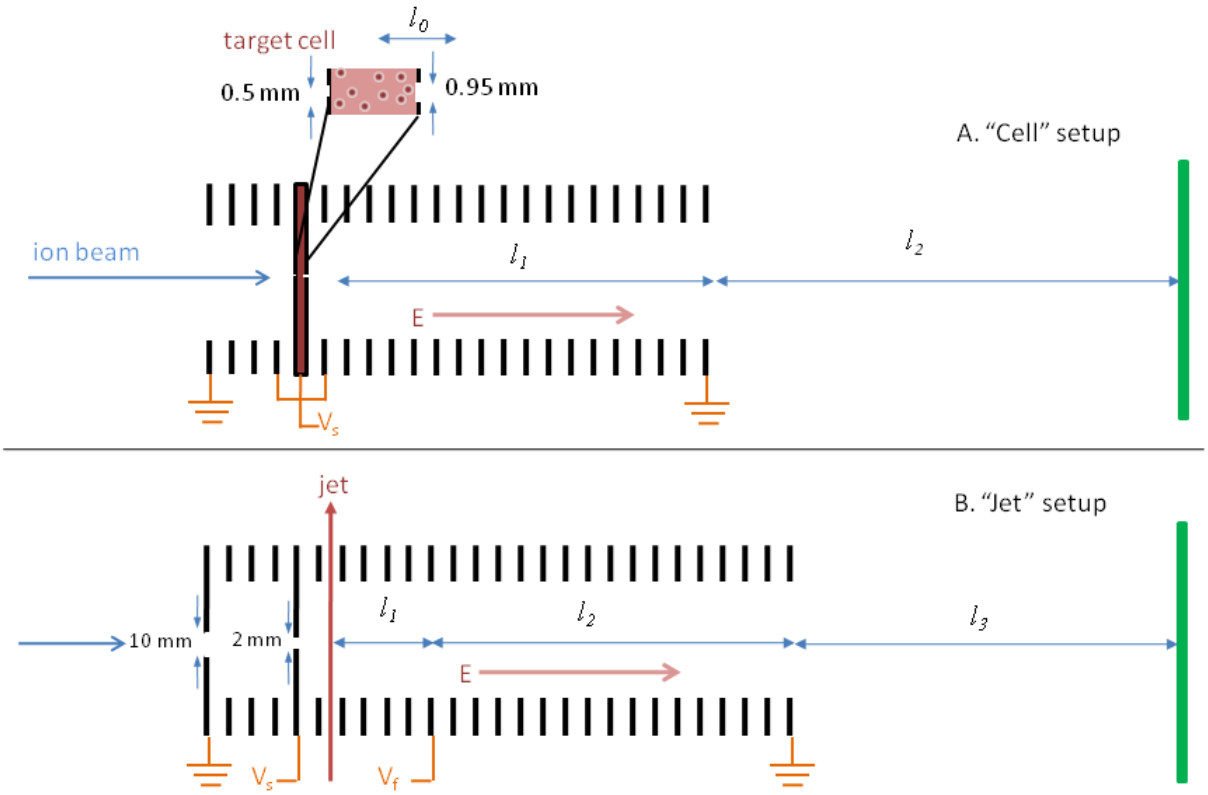

Figure 2.5: Schematic of experimental geometry for (A) the "cell" and (B) the "jet" setups. The voltage as a function of z is shown in Fig. 2.10 for the "jet" setup. Note that V_s is the main spectrometer voltage and V_f is the focusing voltage. See table 2.1 for the other label definitions.

The "cell" spectrometer had a constant electric field gradient following the interaction region (see Fig. 2.5), called "non-focusing" mode. The current setup under discussion has the option of operating in "non-focusing" mode or in "focusing" mode. In focusing mode there is an extra voltage applied to the eleventh ring of the spectrometer. This creates two electric field regions. In the first region there is a strong "extraction" field (about 740 V/cm for $V_s = 2084$ V). In the second region there is a weak "acceleration" field (about 180 V/cm for $V_s = 2084$ V). The focusing spectrometer is used to minimize the effects of the extended target as a source of recoil ions by space and time focusing the recoil ions onto the detector, which is about 800 mm from the interaction region. SIMION simulations were performed to optimize the ratio between the spectrometer voltage and the focusing voltage, defined in Fig. 2.5, in order to get the best resolution in time and position as shown in Fig. 2.6. Under the best conditions, neglecting other experimental resolution limits, δt ~0.05 ns and δx ~0.1 mm for a focus voltage that is 82.6% of the main spectometer voltage.

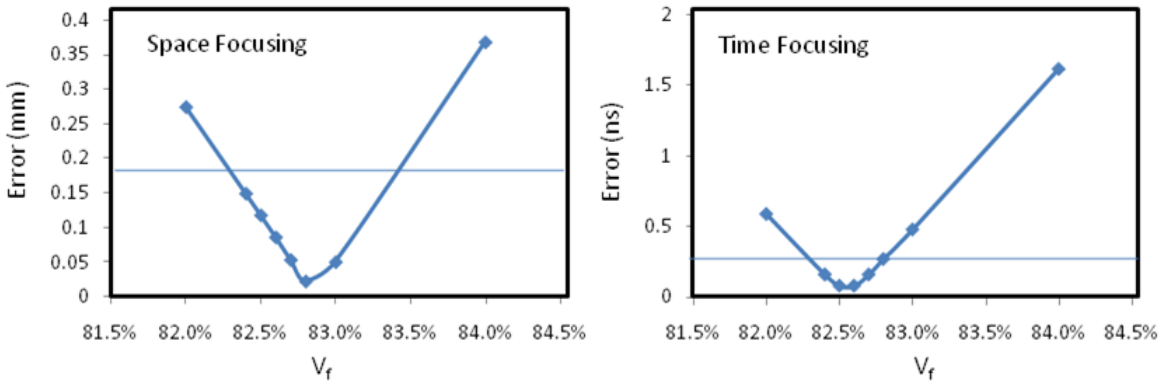

Figure 2.6: Error in space and time focusing as a function of focusing voltage, V_f, where the x-axis labels depict the % of the spectrometer voltage, V_s, which is applied to V_f (the eleventh ring of the jet spectrometer) as simulated with SIMION. The horizontal lines indicate the approximate resolution possible with the current electronics used (see Appendix A).

Tuning the ion beam for the "jet" setup, compared to the target "cell" setup, is much more difficult. In the target cell experiments, one had to tune the ion beam through the small aperture of the gas cell, which ensured overlap of the molecular ions with the target gas.

For the jet setup, however, this guarantee no longer exists because of the many trajectories around the jet. The solution for "finding the jet" with the longitudinal spectrometer was to take advantage of the capture process that can occur when an ion passes by a neutral gas target. A post-spectrometer deflector was used to deflect the ion beam off the beam viewer. The remaining neutralized ion beam signal on the beam viewer is then used to search for the maximum overlap between the ion beam and the jet target. The signature for the best overlap is thus the maximum rate of neutrals from the capture channel.

2.3 Molecular Dissociation Imaging (MDI)

The analysis of the projectiles (also referred to as beam fragments) is the same for both experimental setups. We deal with the projectile analysis first, then in section 2.3.4 we address the recoil ion analysis. The method presented here focuses on diatomic molecular ions impinging on atomic targets, but it can be extended to polyatomic molecular ions if one uses a proper multi-hit detector.

The coordinate system follows the common choice: the z-axis is along the spectrometer axis (approximately along the beam velocity), the y-axis is vertical, the x-axis is horizontal, and the imaging detector is in the xy-plane. The experimental geometry is shown in Fig. 2.5 for both the "cell" and "jet" setups and the variable definitions can be found in Tables 2.1 and C.1.

2.3.1 Field Free MDI

The molecular dissociation imaging equations were first developed for the simplest case, a completely field free setup. Under this condition, the z-axis is chosen to be along the direction of the ion beam propagation.

In the experiment we measure the x and y positions where each of the fragments hit the detector, as well as the time difference between the two hits. The measured quantities, with

velocities given in the projectile center-of-mass reference frame, are:

$$x_1 - x_{cm} = v_{1x}t_1 \tag{2.2}$$

$$y_1 - y_{cm} = v_{1y}t_1 \tag{2.3}$$

$$x_2 - x_{cm} = v_{2_x}t_2 \tag{2.4}$$

$$y_2 - y_{cm} = v_{2_y}t_2 \tag{2.5}$$

$$t_{21} = t_2 - t_1. \tag{2.6}$$

In addition, momentum conservation in the CM system yields

$$m_1v_{1x} + m_2v_{2x} = 0 \Longrightarrow v_{2x} = -\beta v_{1x} \tag{2.7}$$

$$m_1v_{1y} + m_2v_{2y} = 0 \Longrightarrow v_{2y} = -\beta v_{1y} \tag{2.8}$$

$$m_1v_{1z} + m_2v_{2z} = 0 \Longrightarrow v_{2z} = -\beta v_{1z}. \tag{2.9}$$

We can write t_1 and t_2 exactly:

$$t_1 = \frac{l - z_i}{v_{_{0z}} + v_{1z}} \tag{2.10}$$

$$t_2 = \frac{l - z_i}{v_{_{0z}} + v_{2z}} \tag{2.11}$$

where v_{0z} is the average value of the beam velocity at the interaction site and is found by requiring symmetry in v_z, that is v_{1z} and v_{2z} should be centered around 0 in the post collision center-of-mass reference frame.

The unknowns in Eqs. 2.2 – 2.11 are: v_{1x}, v_{1y}, v_{1z}, v_{2x}, v_{2y}, v_{2z}, t_1, t_2, x_{cm}, y_{cm}, z_i, and v_{0z}. They can be solved within the approximation that v_{0z} is taken to be the average value given by $v_{0z} = \sqrt{\frac{2E_b}{M_p}}$ and that z_i is negligible. If we could also measure t_1 in the experiment, we could choose between calculating z_i or v_{0z}.

The DC channel does not require extreme effort to solve exactly for the z-components, namely v_{1z}, v_{2z}, and the times t_1 and t_2 exactly. We start from Eqs. (2.6,2.9, 2.10,2.11). From these equations, the following quadratic equation is derived,

$$\beta v_{1z}^2 + \left[\frac{l}{t_{21}}(1+\beta) + (\beta - 1)\, v_0\right] v_{1z} - v_0^2 = 0 \tag{2.12}$$

from which the solutions for v_{1z} can be found, resulting in:

$$v_{1z} = \frac{1}{2\beta}\left\{-[\frac{l}{t_{21}}(1+\beta)+(\beta-1)v_0]+\sqrt{[\frac{l}{t_{21}}(1+\beta)+(\beta-1)v_0]^2+4\beta v_0^2}\right\}. \tag{2.13}$$

where only the positive sign in front of the square root is physically possible. Once v_{1z} is found, it is simple to find v_{2z} by the relation 2.9. For homonuclear molecules ($\beta = 1$) Eq. 2.13 simplifies to

$$v_{1z} = \frac{l}{t_{21}}\left[\sqrt{1+\left(\frac{t_{21}v_0}{l}\right)^2}-1\right]. \tag{2.14}$$

Once v_{1z}, v_{2z}, t_1 and t_2 are evaluated as above, then the other unknowns can be found as follows:

To solve for v_{1x}, we subtract Eq. 2.4 from 2.2 yielding,

$$x_1 - x_2 = v_{1x}t_1 - v_{2_x}t_2$$

substituting Eq. 2.7 yields

$$x_1 - x_2 = v_{1x}t_1 + \beta v_{1x}t_2 = v_{1x}\left[t_1 + \beta t_2\right],$$

and thus the velocity component along x is

$$v_{1x} = \frac{x_1 - x_2}{t_1 + \beta t_2}, \tag{2.15}$$

and similarly the y velocity component is

$$v_{1y} = \frac{y_1 - y_2}{t_1 + \beta t_2}. \tag{2.16}$$

Adding Eqs. 2.4 and 2.2 yields,

$$x_1 + x_2 - 2x_{cm} = v_{1x}t_1 + v_{2_x}t_2.$$

Substituting Eq. 2.7 yields

$$x_1 + x_2 - 2x_{cm} = v_{1x}t_1 - \beta v_{1x}t_2 = v_{1x}\left[t_1 - \beta t_2\right],$$

thus the center of mass (CM) along x is

$$x_{cm} = \frac{1}{2}\left[(x_1 + x_2) - v_{1x}\left(t_1 - \beta t_2\right)\right], \tag{2.17}$$

and similarly along y is

$$y_{cm} = \frac{1}{2}\left[(y_1 + y_2) - v_{1y}\left(t_1 - \beta t_2\right)\right]. \tag{2.18}$$

Note that, for the homonuclear case, $x_{cm} \neq \frac{1}{2}\left(x_1 + x_2\right)$ but $x_{cm} = \frac{1}{2}\left[(x_1 + x_2) + \frac{x_1 - x_2}{t_1 + t_2} t_{21}\right]$, where $t_1 + t_2 = 2t_0'$ and $t_0' = \frac{l}{v_0}$.

This section is nearly sufficient for describing the DC channel as the field has no effect on neutral fragments. However, without a field, both neutrals and ions will have the same time of flight (TOF). Thus a field is necessary to separate the DC and CID channels. The imaging with a field is developed in the next subsection.

2.3.2 Accelerating Field MDI

As a necessary improvement to the field-free case, the molecular dissociation imaging equations were developed including the electric field provided by the spectrometer. The field is necessary in order to accelerate the charged fragment of the CID products so that the time difference is larger compared to DC. The DC and CID channels are separated in this fashion and there will now be distinct peaks in the time-difference spectrum as shown in Fig. 2.7 for the "cell" measurements and in Fig. 2.8 for the "jet" measurements (where we will address the recoil ion peaks in section 2.3.4). Note that there is an overlap between the two CID peaks in Fig. 2.7. The decision that the event is an H + D^+ or an H^+ + D coincidence relies on calculating the CM in the detector plane of the two fragments assuming both cases are correct. The combination whose CM lies closer to the beam spot on the detector (typically inside the Faraday cup cut) is selected. Therefore we achieve better separation between the two channels compared to using only the time difference information.

Since the DC channel's products are both neutral, the field free imaging formulas would be adequate for describing this channel if we include v_{0x} and v_{0y} factors in the field free

equations of motion to correct for the offset between the beam and the spectrometer field directions, or by redefining the z-axis to point along the beam velocity. For CID, however, the interaction between the charged fragment and the field must now be considered. To begin with, an ideal field – where the field does not extend beyond the spectrometer, i.e. fringe effects are neglected – was assumed. The somewhat more complicated imaging formulas for CID are developed in this section.

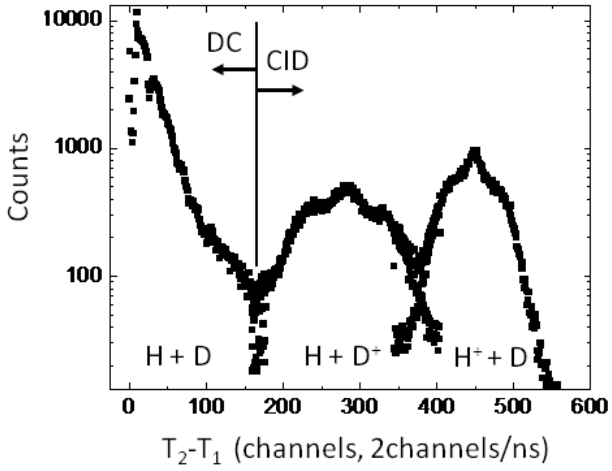

Figure 2.7: Time-difference spectra for 5.5 keV HD^+ on Ar using the cell setup, demonstrating the separation of the DC and CID channels, as well as the two isotopic CID channels.

The extraction field is set such that, for CID, the charged fragment always hits the detector first followed by a second neutral fragment.

In practice, the TOF formulas are solved numerically and therefore exactly. The TOFs for the "cell" setup are now:

$$t_1 = \frac{l_0}{v_{0z} + v_{1z}} + \frac{v_{0z} + v_{1z}}{a}\left[\sqrt{1 + \frac{2al_1}{(v_{0z} + v_{1z})^2}} - 1\right] + \frac{l_2}{\sqrt{(v_{0z} + v_{1z})^2 + 2al_1}} \tag{2.19}$$

$$t_2 = \frac{l}{v_{0z} + v_{2z}}. \tag{2.20}$$

where a is the acceleration due to the extraction field and, again, v_{0z} is the average value of the beam velocity at the interaction site.

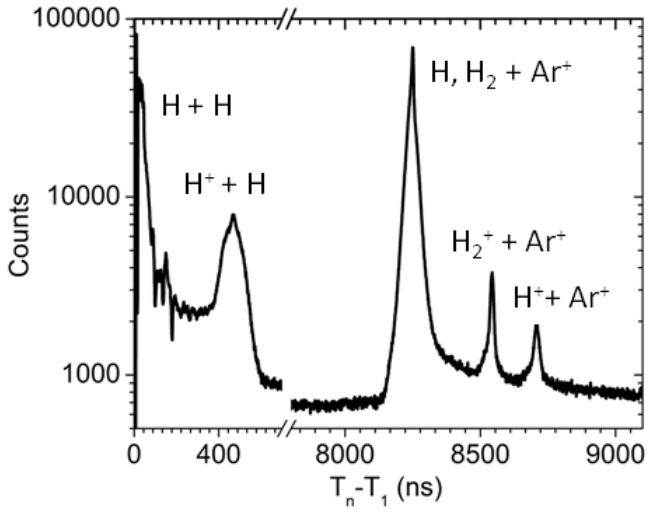

Figure 2.8: Time difference for 1.5 keV/amu H_2^+ on an Ar target with the "jet" setup. The peaks are labelled by the coinciding pairs.

The solution proceeds by first solving for v_{1z}, v_{2z}, t_1 and t_2 using Eqs. (2.6, 2.9, 2.19, and 2.20) for CID. In order to gain some insight about the imaging method, we solve for the time of the first and second fragments in first order in v_{1z}/v_{0z}. First, we rearrange Eq. 2.19 to read:

$$t_1 = t_0 \frac{1}{1+v_{1z}/v_{0_z}} + \frac{v_{0z}}{a}\left[\sqrt{(1+v_{1z}/v_{0z})^2+\eta} - (1+v_{1z}/v_{0z})\right] + \frac{l_2}{v_{0z}\sqrt{(1+v_{1z}/v_{0z})^2+\eta}},$$

where we define η as $\frac{al_1}{\frac{1}{2}v_{0z}^2}$, which in a more convenient form equals $\frac{qV}{\frac{1}{2}Mv_{0z}^2}$, and $t_0 = \frac{l_0}{v_{0z}}$. Expanding all terms in a Taylor series for $u_{1z} \ll 1$, where $u_{1z} = \frac{v_{1z}}{v_{0z}}$, and keeping terms up to first order yields for t_1:

$$t_1 \simeq t_0 + \frac{v_{0z}}{a}\left[(1+\eta)^{\frac{1}{2}} - 1\right] \quad + \frac{l_2}{v_{0z}\sqrt{1+\eta}} - \frac{v_{1z}}{v_{0_z}}\left\{t_0 + \frac{v_{0z}}{a}\left[1-(1+\eta)^{-\frac{1}{2}}\right] + \frac{l_2}{v_{0z}\,(1+\eta)^{\frac{3}{2}}}\right\}.$$

Note that the first line is just the TOF for a charged fragment with $v_{1z} = 0$ denoted as

$t_a = t_0 + \frac{v_{0z}}{a}\left[(1+\eta)^{\frac{1}{2}} - 1\right] + \frac{l_2}{v_{0z}\sqrt{1+\eta}}$. It is convenient to define

$$\rho\, t_a = t_0 + \frac{v_{0z}}{a}\left[1 - (1+\eta)^{-\frac{1}{2}}\right] + \frac{l_2}{v_{0z}\,(1+\eta)^{\frac{3}{2}}}, \tag{2.21}$$

which can be rewritten as

$$\rho \;= \left\{ t_0 + \frac{v_{0z}}{a}\left[1 - (1+\eta)^{-\frac{1}{2}}\right] + \frac{l_2}{v_{0z}\,(1+\eta)^{\frac{3}{2}}} \right\} / t_a \tag{2.22}$$

resulting in the following simple expression for t_1,

$$t_1 \simeq t_a \left(1 - \rho \frac{v_{1z}}{v_{0z}}\right). \tag{2.23}$$

Next, we solve for the velocity in the z direction. For the charged fragment in CID, the velocity, v_{1z}, is calculated in first order using

$$t_{21} = t_2 - t_1$$

where t_1 and t_2 are

$$t_1 \simeq t_a \left(1 - \rho \frac{v_{1z}}{v_{0z}}\right)$$

$$t_2 = t_0' \left(1 - \frac{v_{2z}}{v_{0z}}\right)$$

and

$$v_{2z} = -\beta v_{1z}.$$

Substituting these three equations into the equation for t_{21} and solving for v_{1z}

$t_{21} \simeq t_0' \left(1 - \frac{v_{2z}}{v_{0z}}\right) - t_a \left(1 - \rho \frac{v_{1z}}{v_{0z}}\right) \simeq t_0' \left(1 + \beta \frac{v_{1z}}{v_{0z}}\right) - t_a \left(1 - \rho \frac{v_{1z}}{v_{0z}}\right)$

$\simeq t_0' - t_a + \left(\beta t_0' + \rho t_a\right) \frac{v_{1z}}{v_{0z}}$

yields

$$v_{1z} \simeq v_{0z} \frac{t_{21} - t_0' + t_a}{\beta t_0' + \rho t_a}. \tag{2.24}$$

Then, the times of flight are

$t_1 \simeq t_a \left(1 - \rho \frac{v_{1z}}{v_{0z}}\right) \simeq t_a \left(1 - \rho \frac{t_{21} - t_0' + t_a}{\beta t_0' + \rho t_a}\right) \simeq t_a \frac{\beta t_0' + \rho t_a - \rho t_{21} + \rho t_0' - \rho t_a}{\beta t_0' + \rho t_a}$ which yields

$$t_1 \simeq t_a \frac{(\rho + \beta)\, t_0' - \rho t_{21}}{\beta t_0' + \rho t_a} \tag{2.25}$$

and

$$t_2 = t_0' \left(1 - \frac{v_{2z}}{v_{0z}}\right) \simeq t_0' \left(1 + \beta \frac{v_{1z}}{v_{0z}}\right) \simeq t_0' \left(1 + \beta \frac{t_{21} - t_0' + t_a}{\beta t_0' + \rho t_a}\right) \simeq t_0' \frac{\beta t_0' + \rho t_a + \beta t_{21} - \beta t_0' + \beta t_a}{\beta t_0' + \rho t_a},$$

leading to

$$t_2 \simeq t_0' \frac{(\rho + \beta)\, t_a + \beta t_{21}}{\beta t_0' + \rho t_a}. \tag{2.26}$$

The x and y variables are found in a similar procedure as discussed in 2.3.1 for DC. The difference here is that the z axis was chosen to point in the same direction as the spectrometer. Since there is no guarantee that the beam is also pointing in the same direction as the spectrometer, there are now initial v_{0x} and v_{0y} components that must be accounted for. There are more unknowns (e.g. considering the x direction, variables: v_{1x}, v_{2x}, the initial beam energy in the x-direction, v_{0xi}, and the initial position, x_i) than equations available for solving them (x_1, x_2 and P_x). Therefore, we either replace the unknown initial position (x_i) with its average (x_0) or, we replace the unknown initial velocity (v_{0xi}) with its average (v_{0x}).

The TOF formulas regarding the "jet" setup can be found in Appendix B along with the derivation for the first-order longitudinal momentum for the recoil ions.

2.3.3 Virtual Spectrometer MDI

The formulas developed in the previous section account for an ideal field and corrections to the equations are necessary to account for the aberrations of the real spectrometer.

The idea behind the the virtual spectrometer is to match the TOF formula of an ideal spectrometer to the TOFs evaluated using SIMION simulations (see Fig. 2.9), which are assumed to be "exact" within the experimental uncertainty. This is accomplished by treating the lengths of the spectometer (l_0, l_1 for the "cell" and l_1, l_2 for the "jet") and F, the scaling factor for the acceleration, as fit parameters. This works in principle because we only need to consider that the action on the ions in the field is the same for both cases – virtual and real – which is the same as requiring that the integral of the plots in Fig. 2.10 be the same. The parameters for the "cell" virtual spectrometer are given in Table 2.1. For the purposes

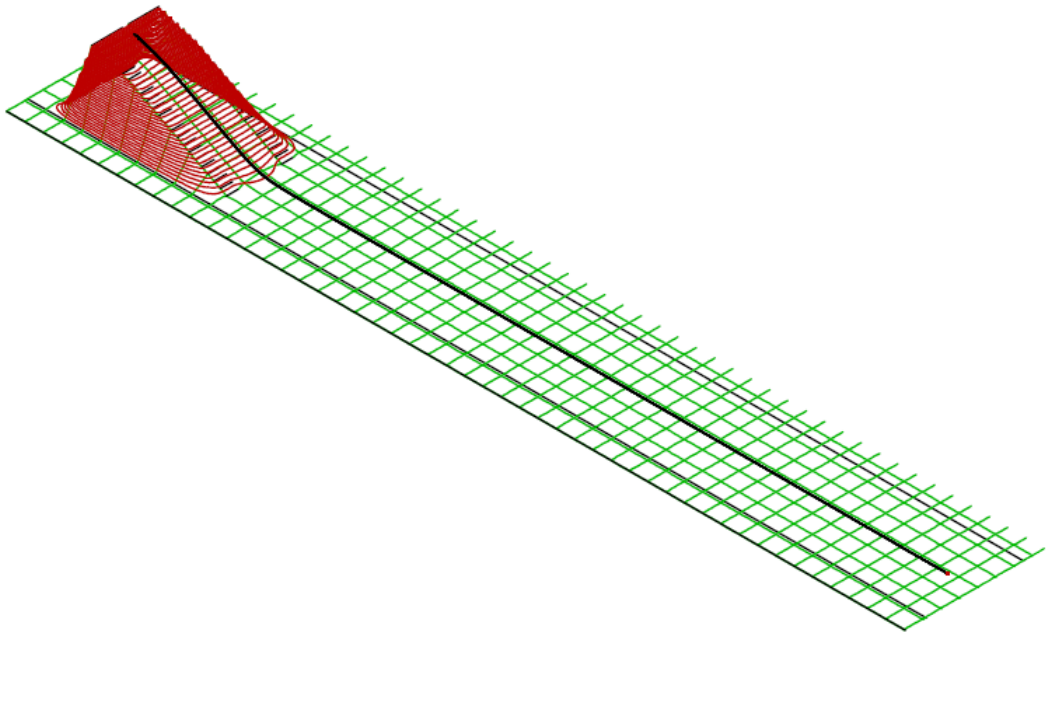

Figure 2.9: Electrostatic potential provided by the longitudinal spectrometer. Red lines are potential contours and the black line represents the trajectory of an ion.

of this thesis, as only one data set was used for demonstrating the capabilities of the "jet" setup, we used the linear TOF approximations.

2.3.4 Recoil Ion Imaging

For the "jet" setup, we have the ability to measure recoil ions and therefore we also obtain the information provided by them. As the jet has an initial velocity upward (for a supersonic argon jet at 1 atm and about 300 Kelvin, the velocity is approximately 323 m/s [31]), it is easily identified on the detector image as shown in Fig. 2.11.

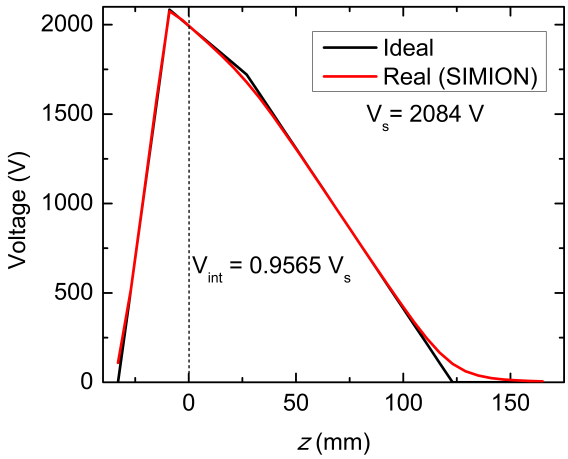

Figure 2.10: The potential along the z-axis of the real (SIMION) and ideal field spectrometer in focusing mode. The goal of the virtual spectrometer is to provide an analytic TOF formula that matches the simulated TOF (SIMION) within the experimental precision. This is accomplished by adjusting the length and F parameters to make the area under the curves for the two plots the same. Note that z=0 mm is defined as the center of the gap between rings six and seven of the spectrometer used for the "jet" setup, as depicted by a dashed line.

2.3.5 Time-of-Flight: Recoil Ions

The TOF of the recoil ions is independent of z_i under proper time-focusing conditions, and is given by the following formula derived from Newton's second law and kinematic equations:

$$t_r = \frac{M_r v_{0z} l_1 F}{q_r V_1}\left[\sqrt{u_{rz}^2+\eta_1'}-u_{rz}\right]+\frac{M_r v_{0z} l_2 F}{q_r V_2}\left[\sqrt{u_{rz}^2+\eta_1'+\eta_2'}-\sqrt{u_{rz}^2+\eta_1'}\right] + \frac{l_3}{v_{0z}}\frac{1}{\sqrt{u_{rz}^2+\eta_1'+\eta_2'}}, \tag{2.27}$$

where again, the variables are defined in Table C.1 and subscript r represents a recoil ion quantity. Also note that for the recoil ion formulas, we use similar notation to the projectile formulas, i.e.

$$\eta_i' = q_r V_i / \left(\frac{1}{2} M_r v_{0z}^2\right), \tag{2.28}$$

where the prime denotes that these constants are associated with the recoil ion.

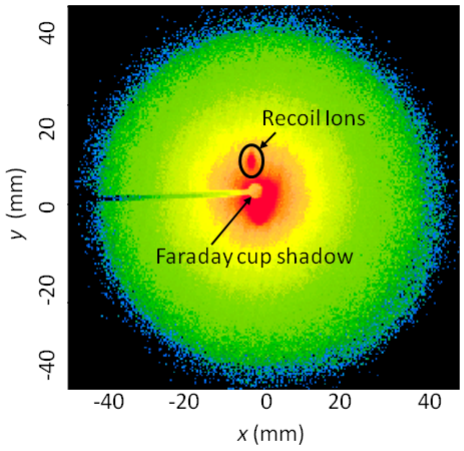

Figure 2.11: x-y position on the detector for "jet" setup after gating on the time-sum of the position wires (for more information see Appendix D of Sayler's Ph.D. thesis [30]).

The expression for t_r above can be rewritten as

$$t_r = \tau_{1r}\left[\sqrt{u_{rz}^2+\eta_1'}-u_{rz}\right]+\gamma\tau_{1r}\left[\sqrt{u_{rz}^2+\eta_1'+\eta_2'}-\sqrt{u_{rz}^2+\eta_1'}\right]+\frac{l_3}{v_{0z}}\frac{1}{\sqrt{u_{rz}^2+\eta_1'+\eta_2'}}, \tag{2.29}$$

where $\gamma = \frac{V_1}{V_2}\frac{l_2}{l_1}$ and defining

$$\tau_{1r} \equiv \frac{M_r v_{0z} l_1 F}{q_r V_1} \ . \tag{2.30}$$

Again, taking advantage of the fact that $u_{rz} \ll 1$ we can expand the TOF formula above as a Taylor series in u_{rz}, which in first order yields,

$$t_r \simeq \left[\tau_{1r}\sqrt{\eta_1'}+\gamma\tau_{1r}\left(\sqrt{\eta_1'+\eta_2'}-\sqrt{\eta_1'}\right)+\frac{l_3}{v_{0z}}\frac{1}{\sqrt{\eta_1'+\eta_2'}}\right]-u_{rz}\tau_{1r}. \tag{2.31}$$

The equation for t_r reduces to

$$t_r \simeq t_{r0} - u_{rz}\tau_{1r}\,, \tag{2.32}$$

where we define the TOF of a recoil "born" at rest (i.e. $u_{rz} = 0$) to be

$$t_{r0} \equiv \left[\tau_{1r}\sqrt{\eta_1'}+\gamma\tau_{1r}\left(\sqrt{\eta_1'+\eta_2'}-\sqrt{\eta_1'}\right)+\frac{l_3}{v_{0z}}\frac{1}{\sqrt{\eta_1'+\eta_2'}}\right]. \tag{2.33}$$

How we determine the Q-value (the Q-value is defined as the difference between the final and initial internal energies of the system, $Q = E_f - E_i$) from the timing information is left for derivation in Appendix B.

2.4 Distortions

Most of the distortions to the data are due to the experimental geometry. As the beam axis and the spectrometer axis are not guaranteed to be the same, an extra effort has to be made to "symmetrize" the data. In the target cell data, since the recoils are not measured, there should be cylindrical symmetry for each channel. The data is corrected by accounting for where the beam points to on the detector face, found from the centroid of x_{cm} and y_{cm}. The indication for well symmetrized data is for the momentum distributions to be centered around zero in the post collision projectile center-of-mass frame.

Another clear distortion is shown in the detector images of Fig. 2.12. As the Faraday cup and the bar that holds it are metallic, this presents a problem for the charged fragments that travel near them, which see their image charge and are therefore deflected towards the bar or cup. Comparing the neutral and charged fragments for CID in H_2^+, we see that the Faraday cup and bar have a distinct outline in the spectra for the neutrals, but they are barely visible for the ions. In the present data, an artificial Faraday cup cut is implemented in order to avoid the distorted data. The distortion due to the metal bar has only been accounted for in the NDTI analysis and should be considered in future analysis of the data for all other channels.

Similarly, to be considered in a final analysis, a different effective artificial cup cut should be implemented for each fragment. For longer flight times, the fragments have more time to expand until they reach the Faraday cup. Therefore, more of these fragments will miss the cup and continue on to be detected than the shorter flight time fragments. In order to consider both cases equally, the cut for the Faraday cup should be larger for longer flight times. Such a consideration is especially important if one is to study isotopic effects where

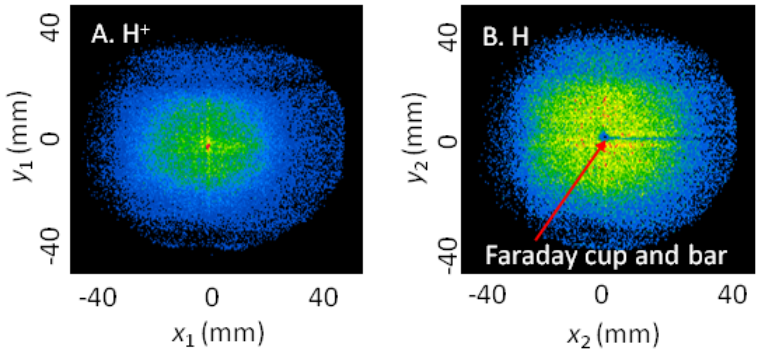

Figure 2.12: Position distribution for the (A) H^+ and (B) H fragments. Notice the H distribution shows the Faraday cup and bar clearly, but the H^+ distribution suffers from distortions due to its image charge for the protons that travel close to the Faraday cup or bar.

the flight times can vary by large amounts.

2.4.1 Artifacts

Unfortunately, experimental limitations can lead to artificial findings in the present work (both setups suffer from artifacts). An example of such an artifact is discussed here.

As the typical experiment is 3 keV H_2^+ on argon, this is the most relevant example for discussion. For such a molecular ion beam, the Faraday cup prevents collection of events with $P_\perp/P_\parallel < 0.003$, where the directionality is with respect to the molecular ion beam's velocity. The KER can be measured up to 8 eV with 4π collection angle for the neutral dissociation products. The small loss of fragments into the Faraday cup or off the edge of the detector does not significantly affect the results of the H_2^+ data.

An experiment using a heteronuclear ion beam may also contain artifacts. A heteronuclear projectile is more susceptible to losses off the edge of the detector, or into the Faraday cup, since the dissociation energy is not shared equally between the fragments due to momentum conservation. This means that the light particle will have a higher dissociation velocity than the heavier particle. This is particularly a problem for HeH^+ as the mass ratio is four. By plotting the position of each hit on the detector (see Fig. 2.13), that is, (x_1,y_1)

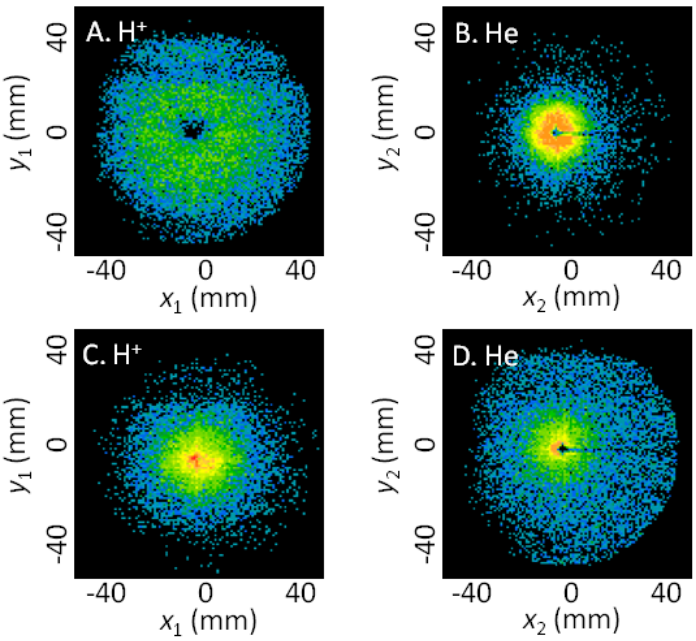

Figure 2.13: HeH^+ mass artifact shown in the position spectra for the He and H^+ fragments. (A) and (B) are for events where the proton goes radially outward. Note the losses of the proton off the edge of the detector. (C) and (D) are for events where the proton goes radially inward. Note the losses/distortions of the proton into the Faraday cup. Recall that the angles are defined from the proton.

and (x_2,y_2) for all events, with the precondition that the charged fragment went outward or inward along the direction of momentum transfer, the artifact is easily seen. One way to avoid or reduce these artifacts is to use an $^3HeD^+$ beam, which reduces the mass ratio to 1.5.

Chapter 3

Dissociative Capture

Dissociative capture (DC) is the dominant channel for few keV H_2^+ collisions with atomic targets [2]. For a generic molecular ion, AB^+, and atomic target, X, DC is the reaction:

$$AB^+ + X \rightarrow A + B + X^+, \tag{3.1}$$

As quantum mechanical processes become more important for low-energy collisions our studies are focused on the few keV energy regime with plans to extend the energy range downward. A slow collision is defined by Nikitin [32] as a collision for which the translational momenta of the electrons can be ignored and is typically satisfied up to hundreds of eV (note that going this low in energy will reduce our detection efficiency dramatically). One result of such slow collisions are angular Stueckelberg oscillations in the differential cross section, a result of interference in two-channel scattering. See Ref. [33] for an example of experimental observation of Stueckelberg oscillations for the double electron capture by 1.5 keV C^{+4} from helium.

Much effort was put forth in the 1980's to grasp the underlying details of DC, with experiments dating back to McClure's in 1965 [10] who studied the angular distribution of the individual dissociation fragments. However, it was the work of de Bruijn *et al.* [3], who implemented a coincidence technique for studying dissociative charge exchange (which we refer to as DC), that shed some light onto the inner workings of this reaction (Eq. 3.1). This group used a clever experimental scheme that allowed them to detect neutral beam

fragments in coincidence. The setup consisted of a gas target cell (1 mm thick) and deflector plates after the interaction region to deflect the beam as well as any charged fragments off their detector. By measuring the flight-time difference and the position of the hits on the detector, they recovered the kinetic energy release (KER) and the angle θ between the axis of molecular dissociation (which is equivalent to the molecular axis within the axial recoil approximation) and the beam velocity. By selecting a cone of angles around $\theta \simeq 90°$ and plotting the 1D KER spectrum, they were able to observe and identify the main contributing process to electron capture, $H_2^+(X^2\Sigma_g^+) \rightarrow H_2(b^3\Sigma_u^+)$, as well as a weaker process involving a predissociating intermediate state, $H_2^+(X^2\Sigma_g^+) \rightarrow H_2(c^3\Pi_u)$. The latter process gives rise to well defined peaks in KER, given high enough experimental resolution, which de Bruijn *et al.* and a few other groups achieved [16, 20].

Curious about a more exotic heteronuclear molecular ion, HeH^+, Wu *et al.* [17] built on the earlier studies and furthered our understanding of the alignment dependence of the dissociative charge transfer process for HeH^+ on He. They employed a coincident beam fragment technique and added a second detector at 90° to the primary beam direction in order to measure the recoil ions. They concluded that the capture process is more likely to occur for HeH^+ ions aligned along their initial (beam) velocity. Our preliminary results on the DC channel of HeH^+ impact on argon agree with Wu *et al.'s* [17] angular distribution.

With a similar setup to Wu *et al.* [17], Saito *et al.* [18] studied dissociative electron capture with target ionization (DECI), a process akin to DC, for 20 keV H_2^+ + Ar. The DECI process is specified as:

$$H_2^+ + Ar \rightarrow H + H + Ar^{+2} + e^-. \tag{3.2}$$

Saito *et al.* find that DECI follows the same KER trends as DC, but DC follows a near-isotropic angular distribution where DECI does not. Since with our "cell" setup we do not measure recoil ions, we cannot distinguish DC and DECI, although we do not expect a large contribution of DECI at a lower collision energy (which was confirmed by the absence of an H + Ar^{2+} peak in the time-difference spectra for measurements of 1.5 keV/amu H_2^+ on

Ar with the "jet" setup). In Fig. 3.1, we directly compare the angular distribution of Saito *et al.'s* results [18] with our results. The angular distributions strikingly disagree, leaving an open question as to why they are so drastically different for a ∼0.4 a.u. change in velocity. Perhaps a future experiment in which the angular dependence of the DC channel is studied as a function of collision energy could shed some light on this curious phenomenon.

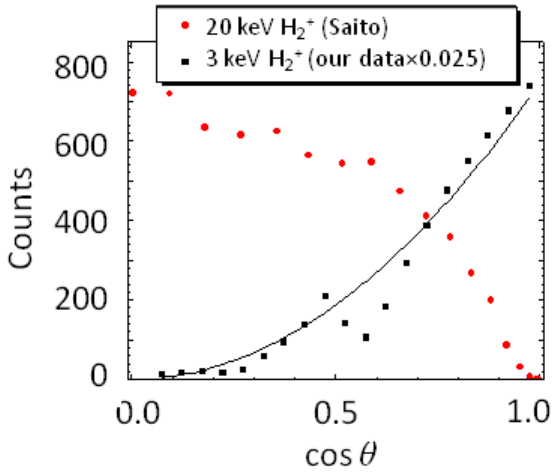

Figure 3.1: Comparison of angular dependence for 3 keV H_2^+ (our data) and 20 keV H_2^+ (Saito *et al.* [18]) on argon for DC. Solid black curve is a $\cos^2\theta$ fit to our data.

Recently, Schmidt *et al.* [19] used the DC channel to study Young-type interference from the scattering of helium atoms off 10 keV H_2^+ (in the moving coordinate frame of the projectile). They were able to map symmetry changes of the electronic wavefunction to an inversion of the fringe pattern and the excitation energy to a phase shift.

Since much interest these days lies in strong field laser interactions with matter (see e.g. reference [34]), it is also interesting to point out a recent experiment by Posthumus *et al.* [20]. They adopted de Bruijn *et al.'s* imaging technique, except that they generated their H_2^+ ions using an intense laser beam. In this way, they studied the vibrational excitation of H_2^+ generated by multiphoton ionization.

The neutral beam fragments can easily be selected for detection by deflecting the charged fragments after the interaction. In previous measurements (e.g. [16, 17]) this was generally

the case. However, with this technique, a direct comparison of the cross section for each channel cannot be made within one measurement. Martínez and Yousif [2] compared DC and CID by measuring H and H^+ fragments. However, their measurements were not coincident, so assigment of the channel is difficult – as both H and H^+ fragments are generated in multiple channels (see reactions 1.1-1.7).

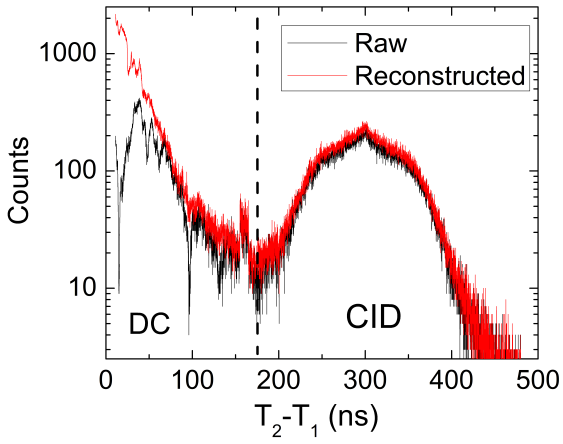

Figure 3.2: Time-difference spectra for 3 keV H_2^+ on argon, black vertical line indicates where the gate was set for considering DC or CID events. The black curve is the raw time difference spectra, and the red curve is after reconstruction of a lost time signal from the position information (details can be found in Sayler's Ph.D. thesis [30]). Note the large gain at very small time differences when reconstructing.

We have developed an experimental setup which allows for longitudinal extraction without deflection of charged species (see chapter 2), allowing simultaneous measurement of DC and CID. Separation of the various reaction channels is outlined in Fig. 3.2, which shows the resulting time-difference spectrum. Recall that this time difference is small for DC and large for CID because of the spectrometer field. A gate is set on the short time difference, and anything which falls into the gate is considered as a DC event. As the background for the "cell" setup was low, this is the only condition that was needed to separate the DC spectra.

For DC, if the molecule breaks perpendicular to its propagation direction, the flight time to the detector for each fragment is the same. Due to a dead time of the electronics used

(mainly the constant fraction discriminator), the second time signal is lost. Fortunately, the two hits will be spread in position, and therefore, the missing time information can be reconstructed from the position (timing) signals. Details on how this is done can be found in Sayler's Ph.D. thesis [30]. The resulting reconstructed spectrum is displayed as the red curve of Fig. 3.2. Note that only the DC channel is dramatically affected by losing a time signal.

Now that we have gated on and corrected the missing time signal problem for DC, we can proceed with the imaging analysis. In doing so, we arrive at Fig. 3.3, which presents the density plot for the correlation of KER and $\overrightarrow{P}_{cm\perp}$, where $\overrightarrow{P}_{cm\perp}$ is the transverse momentum transfer to the center of mass of the molecular ion. We observe that DC occurs mostly at small $\overrightarrow{P}_{cm\perp}$, or in other words, the center of mass is not deflected much and the process can therefore be attributed mostly to "soft" collisions.

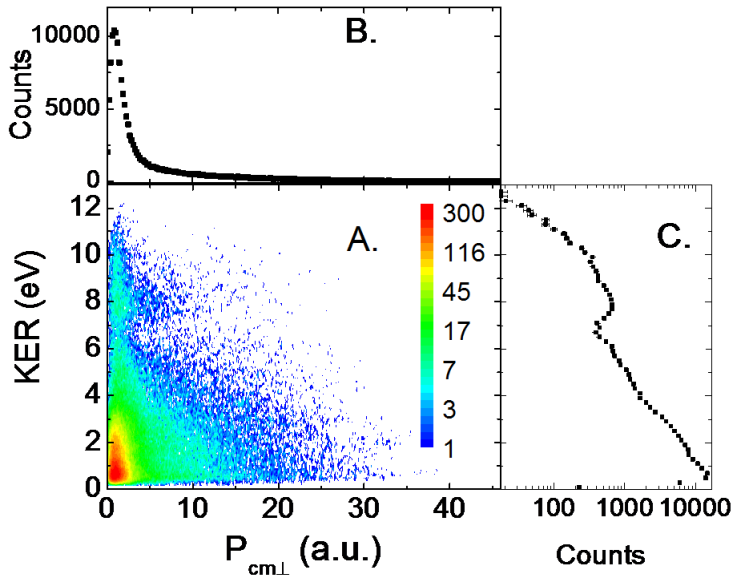

Figure 3.3: (A) Density plot of KER and $\overrightarrow{P}_{cm\perp}$ for the DC channel using the cell setup for 1.5 keV/amu H_2^+ on Ar. Discussion of the high and low KER features can be found in the text. (B) and (C) 1D projection of $\overrightarrow{P}_{cm\perp}$ and KER, respectively.

Despite the majority of the DC process occurring for small $\overrightarrow{P}_{cm\perp}$, there is also a weaker contribution at larger $\overrightarrow{P}_{cm\perp}$ (see the contribution for $\overrightarrow{P}_{cm\perp}$ greater than 5 a.u. in Fig. 3.3).

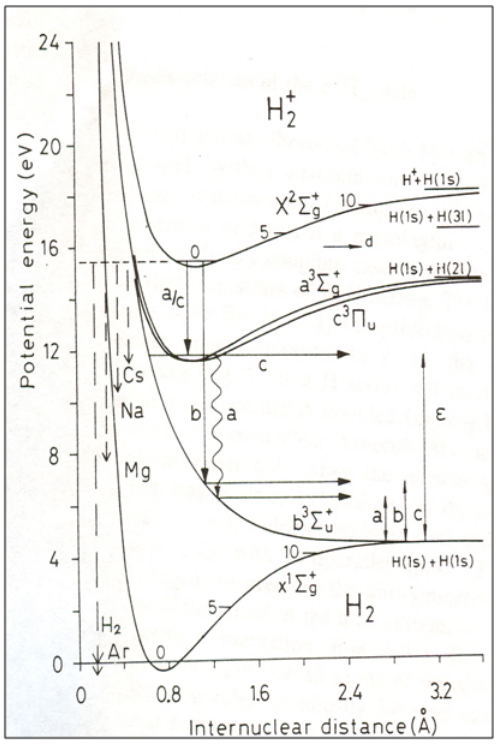

Figure 3.4: Potential energy curves for the lowest states of H_2^+ and H_2, adopted from Ref. [16]. Arrows (a) and (b) depict capture to the $c^3\Pi_u$ and $b^3\Sigma_u^+$ states, respectively, leading to high and low KER. Dashed arrows along the left indicate the ionization potentials of various possible targets, drawn from the lowest vibrational state of H_2^+.

This contribution suggests that DC also occurs at smaller impact parameters, or undergoes "hard" collisons, as expected.

Still referring to Fig. 3.3, we see that the bulk of the contribution to this channel has a large KER range, 0-7 eV. The mechanism for this is direct capture from the ground state of H_2^+ to the repulsive $b^3\Sigma_u^+$ state of H_2, see path (b) in Fig. 3.4. There is also a smaller contribution with KER ∼7-10 eV. The mechanism for this is capture to the $c^3\Pi_u$ state which is coupled to the $b^3\Sigma_u^+$ state and can therefore predissociate – see path (c) in Fig. 3.4. With high enough experimental resolution, vibrational structure of the latter mechanism has been observed [3, 16, 20]. The structures identified in Fig. 3.3 are in good accord with previous measurements.

3.1 Kinematically Complete DC Measurement

Up until this point in the present chapter, only the projectile fragments have been considered, as the measurements were made with the "cell" setup, which does not allow measurement of the recoil ions (i.e. X^+ in Eq. 3.1). To gain kinematically complete information, the recoil ion must be measured, for which we use the "jet" setup. The resulting time-difference spectrum is presented in Fig. 3.5 for 1.5 keV/amu HD^+ on argon. From this spectrum we discern the relevant reactions, given in Table 3.1.

Table 3.1: Reactions involved for 1.5 keV/amu HD^+ collisions with argon.

$HD^+ + Ar$	$\rightarrow$	$H + D + Ar^+$,	(peaks A and E from Fig. 3.5)
	$\rightarrow$	$H^+ + D + Ar$,	(peak C)
	$\rightarrow$	$H + D^+ + Ar$,	(peak B)
	$\rightarrow$	$H^+ + D + Ar^+ + e^-$,	(peaks C, E and H)
	$\rightarrow$	$H + D^+ + Ar^+ + e^-$,	(peaks B, E and G)
	$\rightarrow$	$HD + Ar^+$,	(peak E)
	$\rightarrow$	$HD^+ + Ar^+ + e^-$,	(peak F)

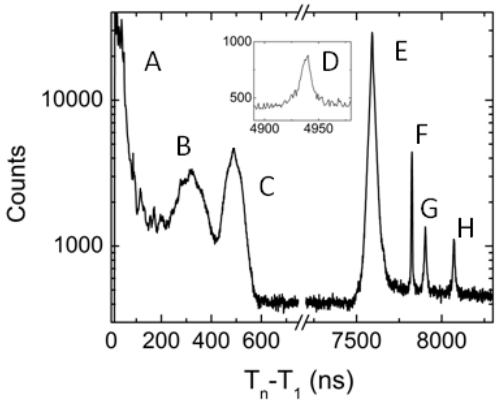

Figure 3.5: Time difference spectra for 1.5 keV/amu HD^+ on argon using the jet stetup. Peak (A) coincidence between H + D (B) H + D^+ (C) H^+ + D (D) un-identified (E) H, D or HD + Ar^+ (F) HD^+ + Ar^+ (G) D^+ + Ar^+ (H) H^+ + Ar^+.

We have chosen HD^+ to demonstrate our method for two reasons. The first is to show that all time difference peaks are cleanly separated (except for peak (E) of Fig. 3.5, which is comprised of all neutral projectiles in coincidence with a recoil ion). The second reason

is to eliminate any doubts that the $H_2^+ + Ar^+$ and $H_2 + Ar^+$ peaks (contributions (F) and part of (E) in Fig. 3.5) might be due to a D^+ contaminant in the H_2^+ beam (i.e. $D^+ + Ar^+$ instead of $H_2^+ + Ar^+$).

Relevant to this section is the DC reaction (Eq. 3.1), where the two neutral beam fragments are detected in coincidence with the recoil ion. This reaction presents itself as two peaks in the time difference spectrum, peaks (A) and (E) in Fig. 3.5. Each peak represents a coincidence: peak (A) is a coincidence between H and D fragments and peak (E) is a coincidence between a neutral (H, D, or HD) and Ar^+. Note, due to detector efficiency and especially due to the dead time of the constant fraction discriminator, where for short time differences the second time signal is easily lost (see Appendix A), the actual number of triple coincidences we collect is less than what is actually occurring. Also, this channel helps to demonstrate the usefulness of taking data in event mode. Briefly, in the initial analysis, two gates are set on the individual peaks (A) and (E), and we require that for a given event, both gates are satisfied. For these events, we plot the KER–$\overrightarrow{P}_{cm\perp}$ spectrum shown previously for the DC data taken with the "cell" setup in Fig. 3.3 and see that the agreement is good.

One of the products of the DC channel is a recoil ion. From the longitudinal momentum of the recoil ion we can determine the Q-value of the reaction [35]. Typical calibration methods for Q-value measurements are to carry out an ion-atom collision with well known Q-values (e.g. see Ref. [36]). This works well for a transverse spectrometer, but is not ideal for longitudinal extraction as it relies on having a large enough transverse momentum transfer for the projectile to escape the Faraday cup. However, it is not impossible, and calibration experiments of this type are underway.

As an alternative to calibrating by the common method, we can use the DC channel for calibration. We know that for capture to the $c^3\Pi_u$ and $b^3\Sigma_u^+$, Q = KER + *constant*. From Appendix B, Eqs. B.39 and B.55, we can relate the Q-value to the time difference. By

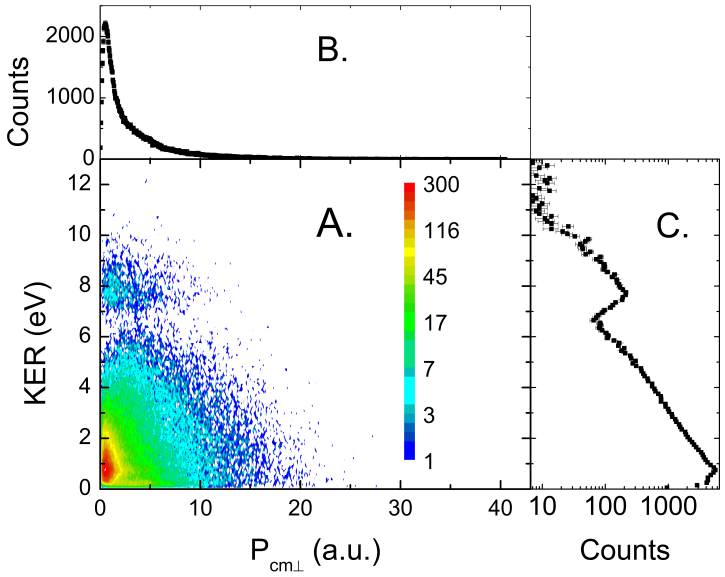

Figure 3.6: (A) Density plot for KER and $\overrightarrow{P}_{cm\perp}$ for DC in 1.5 keV/amu H_2^+ on Ar collisions with triple coincidence requirement. (B) and (C) are the 1D projections onto the $\overrightarrow{P}_{cm\perp}$ and KER axes, respectively.

defining

$$dT = \frac{T_{21}}{\beta_{12}+1} - T_{r1} \tag{3.3}$$

and plugging into the expression for u_{rz} (Eq. B.39) we arrive at

$$u_{rz} \simeq \frac{t_{r0} - t_{n0} + dT}{\tau_{1r} + t_{n0}\beta_{rp}}, \tag{3.4}$$

where

$$\tau_{1r} \equiv \frac{M_r v_{0z} l_1 F}{q_r V_1}, \tag{3.5}$$

$$t_{n0} \equiv \frac{l_1\,(1-z_i') + l_2 + l_3}{v_{0z}}, \tag{3.6}$$

$$t_{r0} \equiv \left[\tau_{1r}\sqrt{\eta_1'} + \gamma\tau_{1r}\left(\sqrt{\eta_1'+\eta_2'} - \sqrt{\eta_1'}\right) + \frac{l_3}{v_{0z}}\frac{1}{\sqrt{\eta_1'+\eta_2'}}\right], \tag{3.7}$$

and T_{21} and T_{r1} are the time differences between the first and second projectile fragments and the first fragment and the recoil ion, respectively. Other variables are defined in Table C.1 in Appendix C.

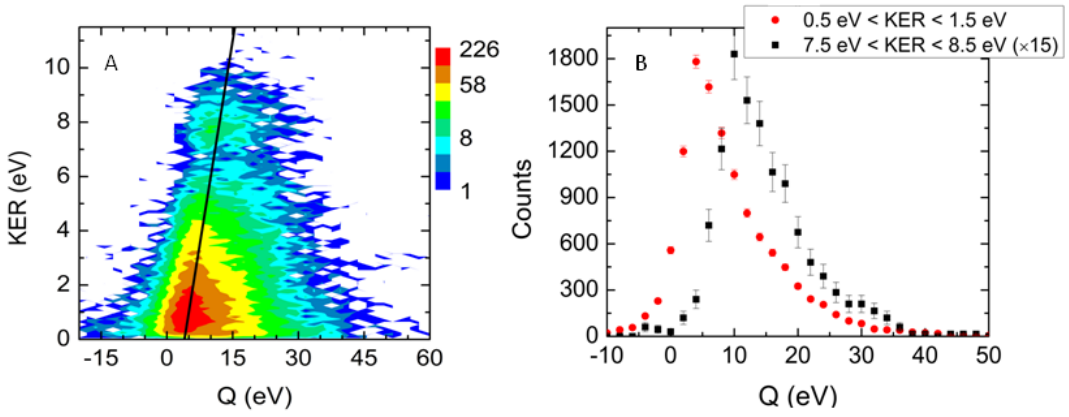

Figure 3.7: (A) Density plot of KER and Q for DC in 1.5 keV/amu H_2^+ collisions with Ar. The drawn line has a slope of one. (B) 1D projections of Q for slices in KER as indicated. The spread in Q comes mainly from experimental factors.

For electron capture, we know from Ref. [37] that

$$Q = v_{0z}P_{\parallel} + n_c\frac{1}{2}v_{0z}^2, \tag{3.8}$$

where n_c is the number of electrons captured. The momentum relation

$$P_{\parallel} = u_{rz}v_{0z}M_r \tag{3.9}$$

can be written as

$$P_{\parallel} = \frac{t_{r0} - t_{n0} + dT}{\tau_{1r} + t_{n0}\beta_{rp}}v_{0z}M_r \tag{3.10}$$

by substituting Eq. 3.4 for u_{rz}. By substitution of Eq. 3.10 into the equation for Q (Eq. 3.8) we finally arrive at

$$Q = \frac{t_{r0} - t_{n0} + dT}{\tau_{1r} + t_{n0}\beta_{rp}}v_{0z}^2M_r + n_c\frac{1}{2}v_{0z}^2. \tag{3.11}$$

This relation can then be simplified to

$$Q = m_q dT + b_q \tag{3.12}$$

where $m_q = \frac{1}{\tau_{1r}+t_{n0}\beta_{rp}}v_{0z}^2M_r$ and $b_q = \frac{t_{r0}-t_{n0}}{\tau_{1r}+t_{n0}\beta_{rp}}v_{0z}^2M_r + n_c\frac{1}{2}v_{0z}^2$.

If we plot KER as a function of dT, a linear relationship between the two quantities is revealed,

$$KER = m_a dT + b_a \tag{3.13}$$

where the subscript a is merely an index to avoid confusion. Solving Eq. 3.13 for dT and substituting into Eq. 3.12, we arrive at

$$Q = \frac{m_q}{m_a} KER + b_q - \frac{b_a}{m_a} m_q. \tag{3.14}$$

Which again reveals the linear relationship between Q and KER. Furthermore, upon comparison of Eq. 3.14 with the previously stated equation for Q, namely $Q = \text{KER} + \textit{constant}$, we see that the slope $\frac{m_q}{m_a}$ must equal one and $b_q - \frac{b_a}{m_a} m_q$ must be equal to the *constant*. We choose the intercept such that the expected Q-values are recovered.

Unfortunately, the Q-value experimental resolution is not well under control yet, resulting in a wide ($>$ 10 eV) distribution as illustrated in Fig. 3.7. The main culprits for the poor resolution are the energy spread of the ion beam, estimated to be about 15 eV full width half maximum, and the accuracy of the power supply readouts for the spectrometer. Possible future endeavors to address the ion beam energy spread are discussed in chapter 7, and initial steps for improving the power supply readout accuracy have been taken. In order to achieve vibrational resolution, the ion beam spread must be lower than a few eV and the voltage supplied to the spectrometer needs to be controllable to within 0.1 volts.

Chapter 4

Collision Induced Dissociation

Collision induced dissociation (CID) for a generic diatomic molecular ion, AB^+, and target atom, X,

$$AB^+ + X \rightarrow A + B^+ + X \text{ or } A^+ + B + X \tag{4.1}$$

results in the breakup of the molecular ion projectile without charge transfer between the collision partners. It is easily separated from the competing dissociative capture (DC) channel in time difference due to the acceleration of the charged projectile fragment by the electric field of the spectrometer. By implementing a gate on the time difference peak for CID, similar to the procedure for selecting only the DC channel as specified in chapter 3 (see Fig. 3.2), we can study the features of this channel separately.

We expect two contributing mechanisms to the CID channel upon inspection of the potential energy curves shown in Fig. 4.1. The red (large) arrow represents an electronic transition (eCID) from the $1s\sigma_g$ ground state to the dissociative $2p\sigma_u$ curve. The KER is equal to the initial vibrational energy plus the amount of energy gained on the dissociative $2p\sigma_u$ curve depicted in the figure as the red (double headed arrow) on the right side of the figure. For the case shown here, the KER is about 0.2 a.u., much larger than the KER shown for the vibrational excitation pathway. The blue (small) arrows represent a vibrational excitation of the molecule. In some cases, there is enough excitation for the molecule to dissociate via the vibrational continuum (vCID). This is the case for the channel under consideration, and the KER is typically small, estimated to be smaller than 0.05 a.u..

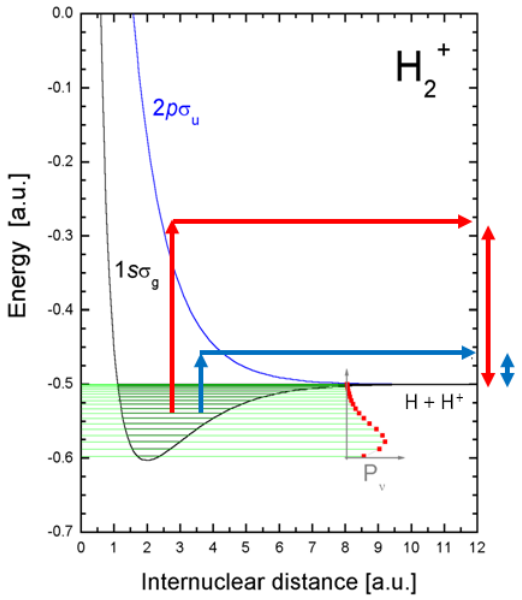

Figure 4.1: Potential energy curves for the two lowest states of H_2^+. The red arrow indicates an electronic transition, depicting eCID, with large KER, and the blue arrow indicates an excitation to the vibrational continuum, depicting vCID, with small KER.

In addition to the expected difference in KER, we also expect that each process occurs for a different impact parameter range. It is well known from previous work [16] that eCID is dominated by "soft," or large impact parameter, b collisions. Likewise, physical intuition leads us to believe that in order for the molecule to be vibrationally excited into the continuum (vCID), large momentum transfer to the nuclei of the system is needed, and therefore the impact parameter must be small. In momentum terms, this translates to small $\overrightarrow{P}_{cm\perp}$ for eCID and large $\overrightarrow{P}_{cm\perp}$ for vCID.

These two distinct differences in KER and $\overrightarrow{P}_{cm\perp}$ are what allow us to cleanly separate the different mechanisms as well as to identify each resulting structure. Given that the KER is related to $\Delta\overrightarrow{P}$ ($\Delta\overrightarrow{P} = \overrightarrow{P}_2 - \overrightarrow{P}_1$, the difference between the dissociation momenta) by KER$\propto \Delta\overrightarrow{P}^2$, we need not calculate KER before we can separate the mechanisms.

So, we sucessfully resolve the CID channel into the processes that give rise to it by studying its basic momentum distributions, $\Delta\overrightarrow{P}$ and $\overrightarrow{P}_{cm\perp}$. A density plot of these two

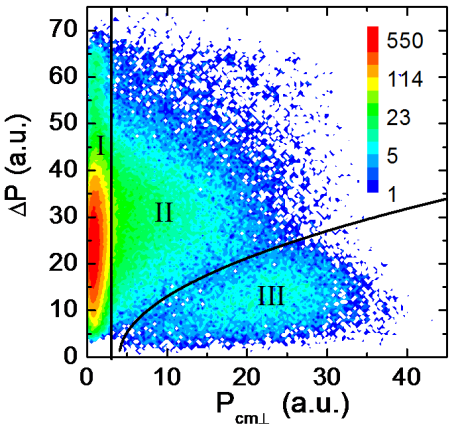

Figure 4.2: A density plot of momentum difference, $\Delta\overrightarrow{P}$, and the transverse momentum transfer to the center-of-mass, $P_{cm\perp}$, for 1.5 keV/amu H_2^+ colliding with an argon target. Structures I and II are identified as soft and hard eCID, respectively, and structure III as vCID. They have ΔP (which is proportional to $\sqrt{KER}$) and $\overrightarrow{P}_{cm\perp}$ as expected for the eCID and vCID mechanisms (see text of this section for further discussion). Black lines indicate the gates used for analysis of the individual mechanisms.

momentum distributions is presented in Fig. 4.2. We observe that, as expected, there are two different mechanisms which comprise this channel (1) electronic excitation from $1s\sigma_g$ to $2p\sigma_u$, called eCID, depicted in the figure as I and II, and (2) vibrational excitation to the continuum of the electronic ground state, called vCID, depicted in the figure as III. Each of these mechanisms leads to the dissociation continuum of the molecular ion.

Referring to Fig. 4.2, feature I extends to large $\Delta\overrightarrow{P}$ and low $\overrightarrow{P}_{cm\perp}$, consistent with what is expected for an electronic transition from $1s\sigma_g$ to $2p\sigma_u$ induced by a large impact parameter collision. These are the signatures of soft collision eCID.

In addition, the feature labelled I has a halo structure, labelled II in the figure. This feature also has large $\Delta\overrightarrow{P}$ and relatively higher $\overrightarrow{P}_{cm\perp}$. It is what one would expect if the molecular ion was electronically excited, after undergoing a close collision with the atomic target, resulting in a higher $\overrightarrow{P}_{cm\perp}$ than in case I. We select events with a $\overrightarrow{P}_{cm\perp} > 2.5$ a.u. to study the "hard" eCID.

Feature III has low $\Delta\overrightarrow{P}$ and high $\overrightarrow{P}_{cm\perp}$. This is consistent with the expected outcome for vCID.

Now that we can cleanly separate the mechanisms of CID, we can study each mechanism individually, and we do so in the following subsections of this chapter.

4.1 Electronic Collision Induced Dissociation – eCID

Electronic CID occurs through the electronic transition from $1s\sigma_g$ to $2p\sigma_u$ for H_2^+ projectiles. A theory based on the Born approximation has been developed by Green and Peek [26], which predicts that for 3 keV collisions between H_2^+ and an Ar target, the dissociation probability will peak for internuclear distance, R, just greater than ~3 a.u. By taking slices in KER, we can use the reflection method [38] to regain the R for which the collision occurred. We compare the results from the theory and the experiment in Fig. 4.3 and find the agreement to be fairly good.

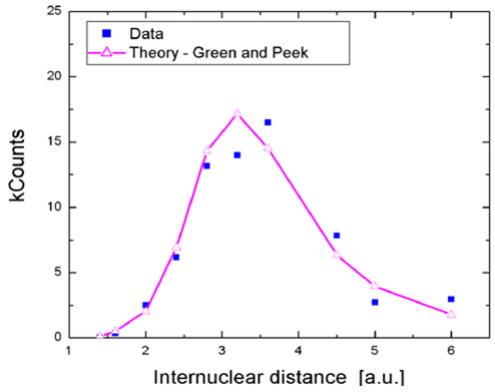

Figure 4.3: Comparison between our 3 keV H_2^+ + Ar data and theoretical calculation done by Green and Peek within the straight line approximation [26]. The data was gated on $\overrightarrow{P}_{cm\perp} < 2.5$ a.u. to select the soft collisions that are better approximated by a straight line trajectory.

Green and Peek also predicted that the alignment angular distribution (θ) varies with R [26]. Again, a slice in KER was taken and converted to the associated R, using the reflection method, in order to compare our experimental results to the predictions of Green and Peek [26]. The resulting distributions for experiment and theory, shown in Fig. 4.4, agree nicely.

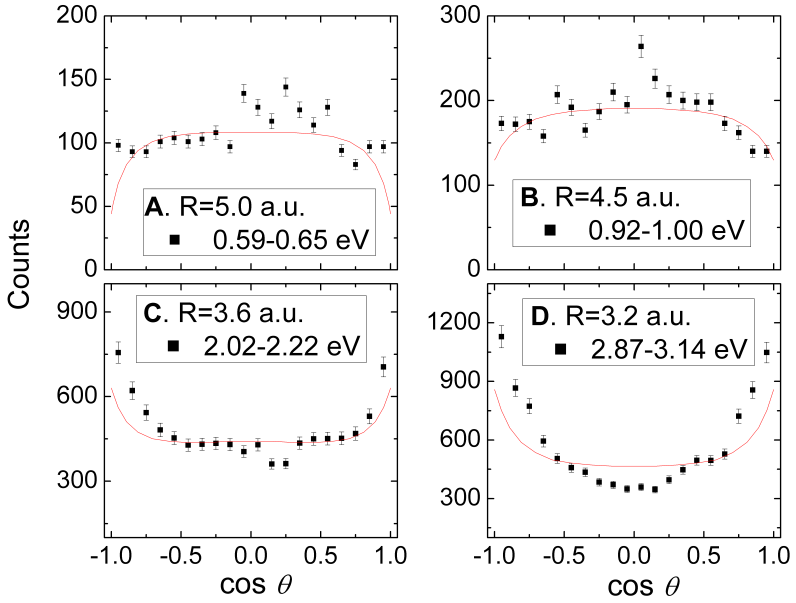

Figure 4.4: Comparison between theory by Green and Peek and our experimental results for the angular dependence of soft eCID (i.e. $\overrightarrow{P}_{cm\perp} < 2.5$ a.u.) for various slices in KER (as indicated on the panels in eV), which correspond to internuclear distances, R. (A) R=5.0 a.u., (B) R=4.5 a.u., (C) R=3.6 a.u., and (D) R= 3.2 a.u. Red lines are the theoretical calculation and data points are experimental results with statistical uncertainty. Note that near $\cos\theta \sim \pm 1$, fragments are lost in the Faraday cup.

4.2 Vibrational Collision Induced Dissociation – vCID

Vibrational CID is an intriguing process, resulting from vibrational excitation to the continuum of the electronic ground state, which was discovered in the late 1960's [4]. It eluded physicists for a while [7] until it was finally correctly identified by Vogler and Seibt [25]. The indication for vCID was a clear feature in the angular distribution (see Fig. 4.5) which could not be described as eCID. However, the two contributions were not well separated with previous experimental techniques and so eCID and vCID could not be studied individually.

As Gibson's [5] data already suggested, great insight is gained by studying the angular distributions for the two CID mechanisms. With full separation of the two mechanisms – as described earlier in this chapter – we can now plot the angular distributions of pure vCID or eCID. We choose our plotting convention in the 2D representation of the angular

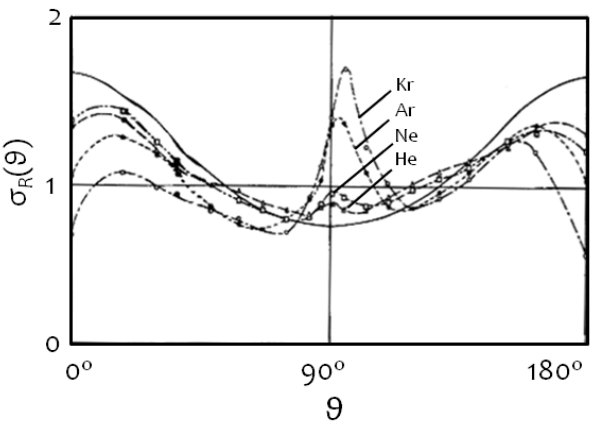

Figure 4.5: Gibson *et al.'s* experimental angular distribution for CID (adopted from [4]) and Peek and Green's Born approximation calculations for eCID (solid line) [10]. The peak at $\theta \sim 90°$, not present in the theoretical line for eCID, is attributed to vCID.

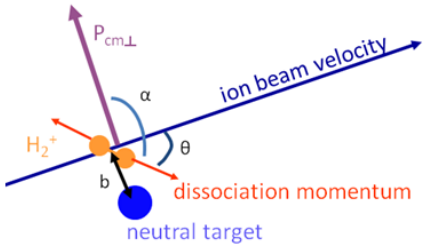

Figure 4.6: Angle definitions for the collision. Both orientation, α, and alignment, θ, angles are measured with respect to the first particle which hits the detector, which is always the charged particle for CID.

distribution to include the angle α – where α is defined as the angle between the molecular dissociation axis and $\overrightarrow{P}_{cm\perp}$ (see Fig. 4.6). A density plot of the cosine of the two angles, θ and α, shown in Fig. 4.7, clearly depicts that eCID and vCID prefer opposite alignments. More specifically, vCID preferentially breaks when the H_2^+ is aligned perpendicular to the beam direction and parallel to $\overrightarrow{P}_{cm\perp}$ while eCID prefers to break when the H_2^+ is aligned parallel to the beam direction and perpendicular to $\overrightarrow{P}_{cm\perp}$. Note that all analysis was done within the axial recoil approximation [39].

The preference in angles for vCID becomes more clear if we consider the process as two independent proton-argon scattering events, as depicted schematically using a "ball-

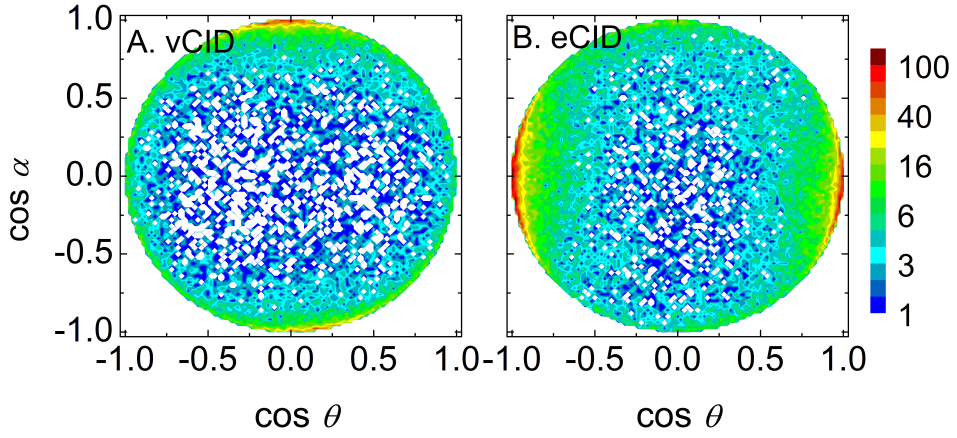

Figure 4.7: Contrast between H_2^+ "hard" eCID and vCID (gates marked II and III in Fig. 4.2, respectively) in angular distribution. Note the striking difference in alignment for eCID versus vCID and see text for discussion.

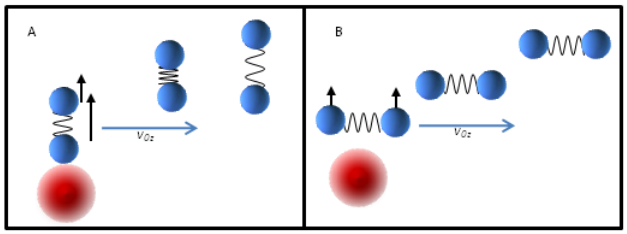

Figure 4.8: Ball-and-spring model describing the angular dependence for the eCID and vCID mechanisms. Panel (A) shows that vCID prefers to dissociate perpendicular to the beam direction and parallel to $P_{cm\perp}$, while panel (B) shows that eCID prefers to dissociate parallel to the beam direction and perpendicular to $P_{cm\perp}$. Qualitatively, for the same impact parameter, the closer molecular nucleus in vCID is kicked harder than the further nucleus resulting in larger vibrational excitation. In contrast, for eCID, each nucleus receives the same amount of kick and therefore does not get vibrationally excited.

and-spring" model in Fig. 4.8. For a small impact parameter, if the molecule is aligned perpendicular to its direction of motion, the closer proton will acquire more transverse momentum transfer than the far proton. Such a scenario results in large vibrational excitation (large $\Delta\overrightarrow{P}$) which will lead to dissociation via the vibrational continuum. In contrast, a molecule aligned parallel to the beam direction can be deflected to a large angle without breaking unless the electron is excited.

4.3 vCID for H_2^+ and HeH^+

One interesting question to ask is: how do eCID and vCID compare for a molecular ion with significantly different electronic structure than H_2^+? A molecular ion such as HeH^+ has a ground state that is well separated from the excited dissociative curves as shown in Fig. 4.9.

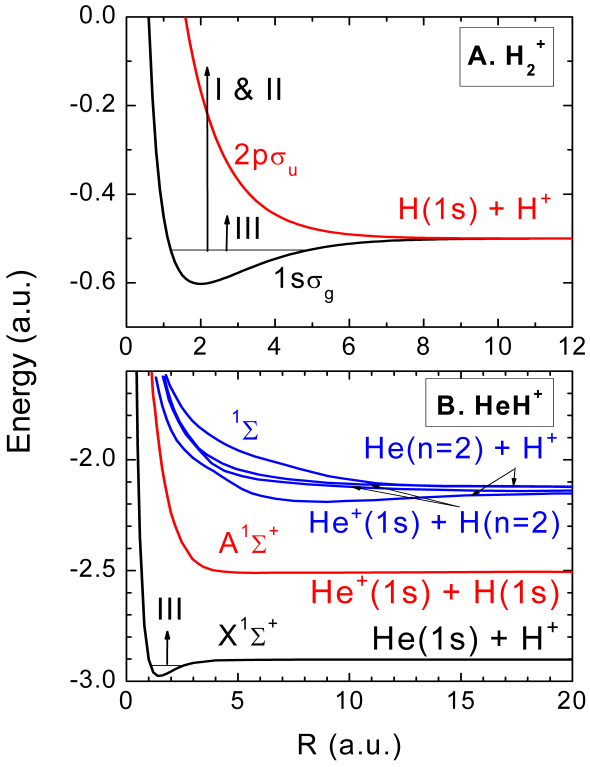

Figure 4.9: Potential energy curves for the low lying states in (A) H_2^+ and (B) HeH^+. For both cases, the arrows labeled III indicate a transition to the vibrational continuum and the arrow labeled I and II indicates an electronic transition. The HeH^+ curves are adopted from Ref. [40].

As HeH^+ is a heteronuclear molecule, it has the option of breaking into He^+ + H or He + H^+ to comprise the CID channel. If we investigate the potential energy curves, however, we realize that, starting in the electronic ground state of HeH^+, the He^+ + H channel requires an electronic transition to the $A^1\Sigma^+$ curve before it can dissociate to the He^+ + H continuum. Therefore, we do not consider it as pure vCID and only compare the He + H^+

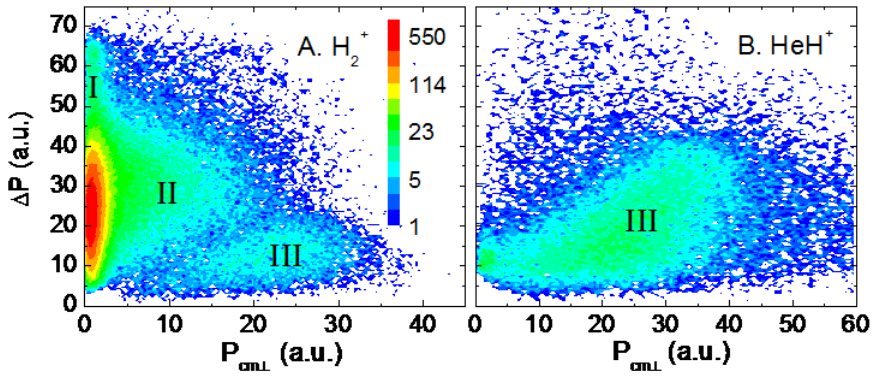

Figure 4.10: Density plot of $\Delta\overrightarrow{P}$ and $\overrightarrow{P}_{cm\perp}$ for 1.5 keV/amu (A) H_2^+ and (B) HeH^+ impact on Ar. The features marked I-III are the same as in Fig. 4.2. Note the absence of eCID for HeH^+.

channel to the H_2^+ results.

First, we compare the momentum distributions, shown in Fig. 4.10, and notice a remarkable difference between panels (A) and (B). The eCID, which dominates the H_2^+ dissociation, is nearly non-existent for HeH^+. Investigating the potential energy curves in Fig. 4.9, we see that the energy gap between the $1s\sigma_g$ and $2p\sigma_u$ states of H_2^+ is much smaller than it is between the $X^1\Sigma^+$ state and the repulsive $^1\Sigma$ states leading to the He + H^+ dissociation limit. Therefore, in order to excite the electron by the $\sim$1 a.u. needed to reach these curves for HeH^+, the collision has to be rather violent, i.e. the impact parameter b must be small.

Furthermore, we find that not only is eCID suppressed in HeH^+ compared to H_2^+, our data suggest that the vCID in HeH^+ is enhanced. The cross section for vCID in HeH^+ is estimated to be an order of magnitude greater than for H_2^+. This enhancement is attributed to the nuclear charge differences between the two molecular ions. The heteronuclear HeH^+ is more easily excited vibrationally as the mismatch in momentum transfer to each individual nuclei, due to the asymmetry in nuclear charge, is greater than for a homonuclear molecule.

The density plots of $\cos\theta$ and $\cos\alpha$ are shown in Fig. 4.11 for HeH^+ and H_2^+. From panels (A) and (C) we see that what we have identified as vCID from H_2^+ (A) and HeH^+ (C) prefer similar alignment, as we would expect from the "ball-and-spring" model. Note

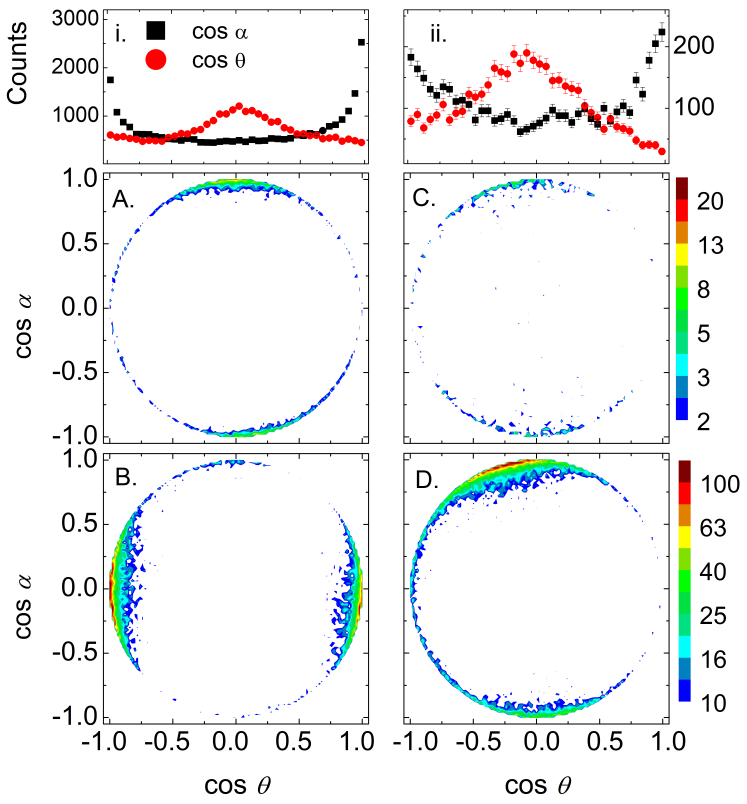

Figure 4.11: (A-D) Density plots of $\cos\alpha$ vs. $\cos\theta$ for H_2^+ (A) vCID and (B) eCID, and HeH^+ (C) vCID with the condition 41 a.u.$< \overrightarrow{P}_{cm\perp} <$ 51 a.u. and (D) for all vCID. Panels (i) and (ii) are the 1D projections of (A) and (C), respectively. Note the agreement among the vCID distributions and the general disagreement between the eCID distribution and all of the vCID distributions. The upper color scale is for panel (C), and the lower is for all other 2D plots.

that for panel (C), only counts which fall within 41 a.u. $< \overrightarrow{P}_{cm\perp} <$ 51 a.u. are considered as this region suffers less from proton losses – this artifact is described in subsection 2.4.1.

4.4 CID "Jet" Setup

Using two methods, namely the "cell" and "jet" (which enables the measurement of recoil ions) techniques, we can verify the reproducibility of our measurements. For CID, by comparing the data for H_2^+ from the "cell" setup in Fig. 4.2 and from the "jet" setup in panel (A) of Fig. 4.12, we see that the separation between eCID and vCID is much worse

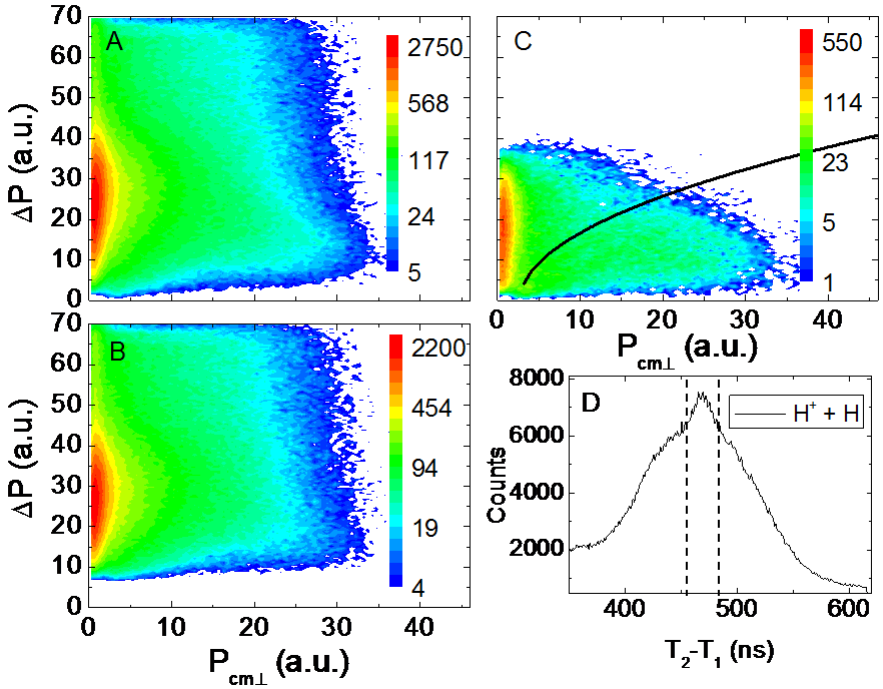

Figure 4.12: Density plot of $\Delta\overrightarrow{P}$ versus $\overrightarrow{P}_{cm\perp}$ for the CID channel of 3 keV H_2^+ colliding with argon (A) for 350<T_n-T_1<600 (B) for 350<T_n-T_1<465 and 482<T_n-T_1<600 (the wings) (C) for 465<T_n-T_1<482 (times are in ns). The black line in panel (C) depicts the gate used to further separate the vCID from the eCID contributions. Panel (D) shows the time difference peak for the CID channel, along with the gate (dashed black lines) to make plots (B) and (C) using the "jet" setup. See text for further explanation.

in the data taken with the "jet" setup. The reason for the worse separation is the higher beam divergence in the "jet" experiment, therefore smearing together the eCID and vCID features in the momentum plot. As this is the case, it becomes less straightforward to set gates on the $\Delta\overrightarrow{P}$ versus $\overrightarrow{P}_{cm\perp}$ plot in order to separate eCID from vCID. However, we can use what we learned from the "cell" results to help guide the process. In both methods, we see a narrow peak in the center of the CID fragment coincidence time-difference spectrum (see Figs. 3.2 and 2.8), which we have identified with the vCID mechanism. Hence, if we set a gate on the narrow peak of the time-difference spectrum (see panel (D) of Fig. 4.12), then we can be assured to have a better chance of resolving the vCID and eCID, as shown in panels (B) and (C) of Fig. 4.12. Mainly eCID appears in panel (B), and in panel (C),

eCID is suppressed compared to vCID, therefore a clearer distinction can be seen between the two contributions, allowing us to better separate them.

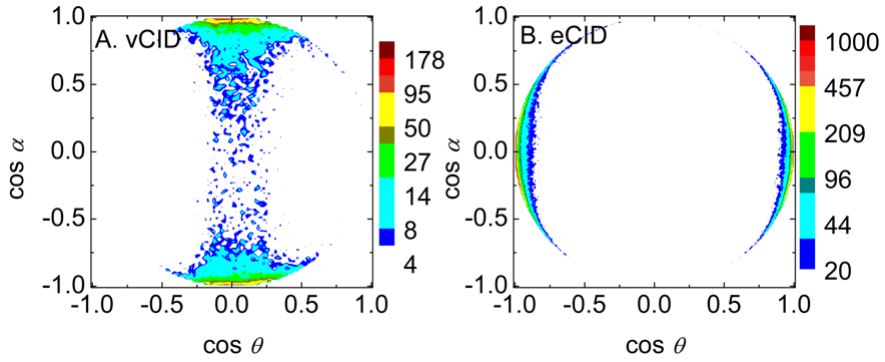

Figure 4.13: Contrast between H_2^+ (A) vCID and (B) eCID angular distributions of 3 keV H_2^+ on Ar for the "jet" setup. Note the striking difference in alignment for eCID versus vCID.

We can then plot the angular distributions, shown in Fig. 4.13 where panel (A) is vCID and panel (B) is eCID (respectively, the lower and upper cuts in panel (C) of Fig. 4.12). Both distributions exhibit the same behavior as the ones measured with the "cell" setup.

As the resulting momentum and angular distributions are similar, we are confident in our measurement with reproducible data using two different methods. As the quality of these distributions is not as good in the "jet" setup as in the "cell" setup due to the beam divergence in the former case, it would be worthwhile to improve the experimental apparatus in order to reduce the problem. The beam is well collimated in the "cell" setup because it must pass through the small aperture of the target cell and must also enter the small Faraday cup, about half a meter away. This is not the case with the open geometry of the "jet" setup. The beam is still directed to the Faraday cup, but there is no guarantee that the beam is not being focused there. If this is the case, the beam is larger at the interaction region and therefore not collimated. A possible solution would be to place a removable aperture in front of the jet (much like an iris when aligning a laser), and then use it to help align and collimate the ion beam.

4.5 Collision Induced Dissociation–Target Ionization

An interesting question to ask, now that we have a better understanding of vCID and eCID, is: is it possible to ionize the target in this process and, if so, by what mechanism? The three possible mechanisms which result in collision induced dissociation–target ionization (CID-TI) are: (1) electron capture to an autoionizing state of H_2,

$$H_2^+ + Ar \rightarrow H_2^{**} + Ar^+ \rightarrow H^+ + H + Ar^+ + e^- \tag{4.2}$$

(2) CID with target excitation to an autoionizing state,

$$H_2^+ + Ar \rightarrow H^+ + H + Ar^{**} \rightarrow H^+ + H + Ar^+ + e^- \tag{4.3}$$

and (3) direct target ionization

$$H_2^+ + Ar \rightarrow H^+ + H + Ar^+ + e^-. \tag{4.4}$$

However, direct target ionization is typically negligible at these collision velocities (see scaled cross section given in Fig. 3 of [41] for a reduced velocity of about 0.2 a.u., where an effective charge of 1.7 a.u. for H_2^+, and a 0.25 a.u. velocity are considered). In order to truly determine which mechanism gives rise to CID-TI, we need to determine the Q-value for the reaction. However, experimental improvements, discussed in chapter 7, would need to be made first.

Upon first inspection of the vCID and eCID mechanisms, it seems that if a recoil ion were to be generated in one of them, it would more likely be for vCID, where we know that the collision has to be extremely close based on previous findings (see Fig. 4.2). Therefore, it seems logical to compare CID-TI to vCID.

Since a recoil ion is produced in CID-TI, we require a triple coincidence (among two beam fragments and a recoil ion), and we impose momentum conservation between the center of mass of the fragmented molecule and the recoil ion to further clean the data. For the H^+ + H, we make a 2D plot of $\Delta\overrightarrow{P}$ and $\overrightarrow{P}_{cm\perp}$ (shown in Fig. 4.14) and use the same cleaning gates as before to generate the angular distributions shown in Fig. 4.15. Comparing this

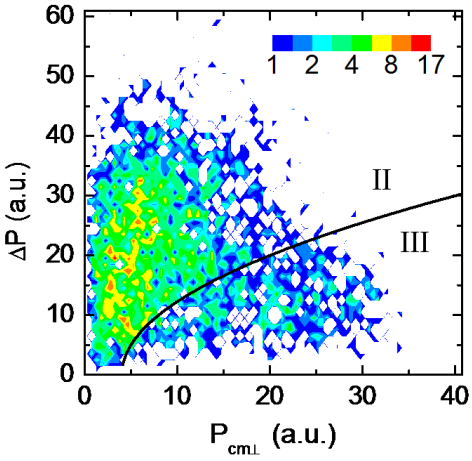

Figure 4.14: Density plot of momentum difference, $\Delta\overrightarrow{P}$, versus transverse momentum transfer to the center of mass, $\overrightarrow{P}_{cm\perp}$, for the molecular dissociation of the CID-TI channel. Note the cut dividing the figure into upper (eCID-TI) and lower (vCID-TI) sections is the same as the cut used to separate eCID and vCID for the CID channel (see Fig. 4.12 C).

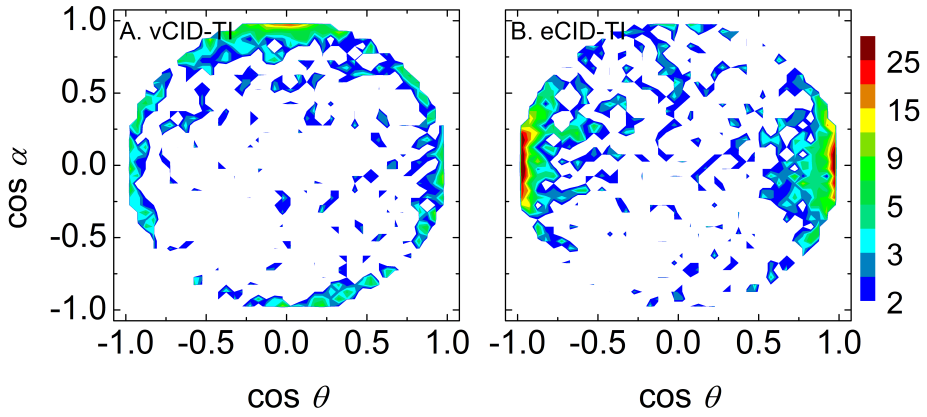

Figure 4.15: Angular distributions for (A) vCID-TI and (B) eCID-TI. Note the general agreement with Figs. 4.7 and 4.13, and the disagreement for vCID-TI at $\cos\alpha = -1$ which is discussed in the text.

figure with those from the "cell" and "jet" CID angular distributions (Figs. 4.7 and 4.13, respectively), we see that, in general, they look the same. The only difference is that for vCID-TI, there is a strong preference for $\cos\alpha = 1$ over $\cos\alpha =$ -1. We speculate that this orientation effect arises from the long range Coulomb interaction between the proton and recoil ion after the collision. Sticking to the ball-and-spring model (discussed in section 4.2), we expect that the Coulomb interaction would be the greatest when the proton is

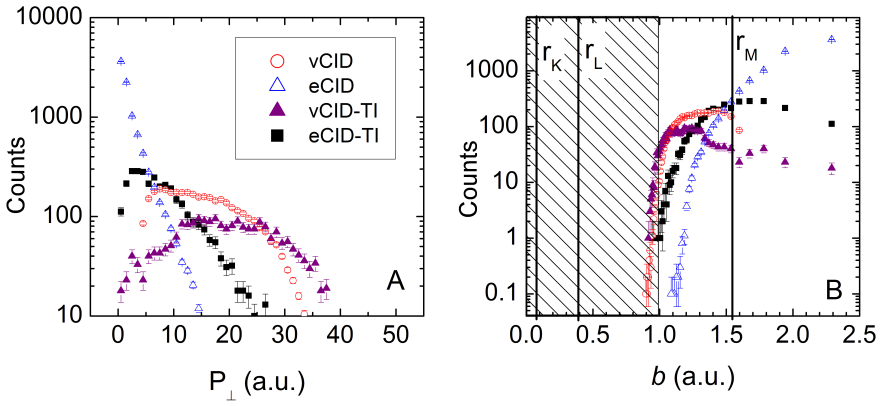

Figure 4.16: (A) Transverse momentum and (B) impact parameter distributions for vCID, eCID, vCID-TI and eCID-TI. The weighted averages for the electronic shell radii for the argon atom are shown in (B) as vertical lines, and the shaded area is the width of the L shell, defined approximately as the weighted average ±3 standard deviations.

the closer collision partner (recall that the angular preference is perpendicular to the beam direction and parallel to $\overrightarrow{P}_{cm\perp}$). Depending on the strength of the interaction, the proton could be deflected further than the hydrogen atom, and would therefore appear as an event where the proton was the further collision partner with the target (i.e. $\cos\alpha = 1$). Previous studies using highly charged ions have shown similar effects, (e.g. see Refs. [42] and [43]). Calculations need to be undertaken in order to quantify how large the interaction between the proton and the recoil ion really is to see if this argument can explain the observed orientation effect.

It is also interesting to compare the impact parameter, b, ranges for which CID-TI and CID occur. Since we cannot experimentally determine b, we have to assume a model. We chose an exponentially screened Coulomb potential model which relates $P_\perp$ to b by:

$$\theta_{cm} = \frac{P_\perp}{P_\parallel} = (\alpha_{sc} q_1 q_2 / E) K_1(\alpha_{sc} b) \tag{4.5}$$

where K_1 is a modified Bessel function of the second kind, and we used a screening length of $\frac{1}{\alpha_{sc}} = 0.35$ a.u. for argon, as determined from Ref. [44]. To simplify the conversion, we treated the H_2^+ projectile as a single particle with an effective nuclear charge of 1.7 a.u.

The resulting distribution for b is shown in Fig. 4.16. Also in the figure are the weighted average values for the K, L, and M shell sizes of argon with the width of the L shell given by ($\pm$) three standard deviations, where $<r>$ and $<r^2>$ are taken from Ref. [45]. The b distribution suggests that the molecular ion passes though the M shell and into the L shell.

Chapter 5

Non-Dissociative Processes

The experimental technique presented in this thesis was designed for channels involving molecular dissociation. However, the technique also applies to channels where the molecular projectile does not dissociate, given that it has a large enough scattering angle to escape the Faraday cup. We briefly visit the non-dissociative processes in this chapter.

Non dissociative processes for a generic diatomic molecular ion, AB^+, and target atom, X, include non-dissociative capture (NDC) and non-dissociative target ionization (NDTI), explicitly given by

$$AB^+ + X \rightarrow AB + X^+, \qquad \textbf{NDC} \tag{5.1}$$

$$\rightarrow AB^+ + X^+ + e^-. \qquad \textbf{NDTI} \tag{5.2}$$

5.1 Non-Dissociative Capture

Non-dissociative capture results in a neutral molecule and a recoil ion (see Eq. 5.1) and appears in the same time-difference peak as a neutral fragment and a recoil ion. Therefore a time-difference gate alone is insufficient for identifying true NDC events. Since NDC suffers from contamination by non-NDC events, a more detailed discussion on the analysis is presented followed by the results.

5.1.1 Data Analysis

As the time difference peak for a neutral and a recoil ion coincidence is shared for H and H_2, we require additional tests to identify true H_2 + Ar^+ events. The main difference between the events falling in the neutral plus recoil ion time-difference peak is that a recoil ion in coincidence with H_2 will conserve momentum where a recoil ion in coincidence with an H (neutral fragment) will not. Therefore, requiring transverse momentum conservation will drastically reduce the non-NDC events.

The transverse momentum distributions for H_2 and Ar^+ are shown, respectively, in panels (A) and (B) of Fig. 5.1 for the whole time-difference gate. Note that the recoil ion distribution appears asymmetric in x because of the losses of projectiles into the Faraday cup. Also note that the elongation of the recoil ion distribution in y is due to the velocity distribution of the jet that points in this direction. For these collisions, the ϕ distribution is expected to be symmetric. In order to achieve a symmetric ϕ distribution, a bow-tie cut, favoring the geometrically cooled x direction is applied (the diagonally hashed sections are not considered). Due to the large losses of projectiles into the Faraday cup, only half of the remaining distribution is considered (the horizontally hashed sections are not considered).

Since NDC is meaningless for $P_\perp$ less than a few a.u. due to losses in the Faraday cup (or bar), another ϕ gate is set to eliminate this contribution. These ϕ gates are shown in Fig. 5.1 as the vertically hashed sections for both projectile and recoil ion distributions. The remaining events are then considered as true NDC.

The events which are considered to conserve momentum in the x direction are shown in panel (B) of Fig. 5.2. Note that events outside the gate are not shown and a similar gate is set for the y momentum distribution, which is not shown for conciseness. The resulting ϕ distribution (plotted against the transverse momentum of the recoil ion), considering these gates, is flat as shown in panel (A) of Fig. 5.2.

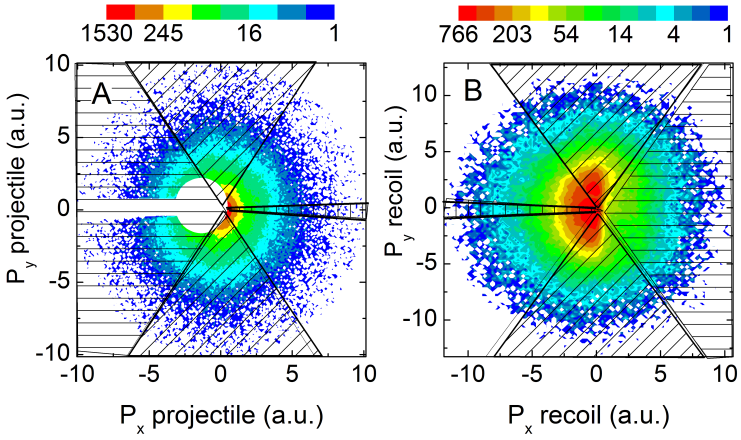

Figure 5.1: Transverse momentum distribution for the (A) projectile and (B) recoil ion for the NDC channel. Slanted hashes denote the sections of the distribution not considered due to broadening caused by the jet velocity spread along its axis. Horizontal and vertical hashes are excluded due to distortions by the Faraday cup and bar.

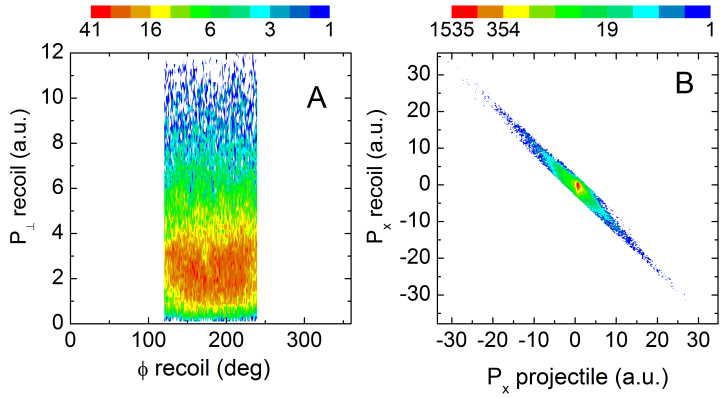

Figure 5.2: Density plots of (A) the transverse momentum, $P_\perp$ recoil, and azimuthal angle, ϕ, for the recoil ion and (B) x momentum for the recoil ion and the projectile showing momentum conservation. Note that these distributions have all cuts discussed in Fig. 5.1, except the vertically hashed section, and also that the selected events are uniform in ϕ.

5.1.2 Results

Obviously, electron capture from the target to the molecular ion projectile is the only reaction mechanism responsible for NDC. Therefore it is logical to compare NDC and DC. Since KER, alignment, and orientation are not accessible quantities for non-dissociative events, $P_\perp$ is the only quantity which we can directly compare. We see in Fig. 5.3 that the $P_\perp$ agrees well for capture to the predissociative $H_2(c^3\Pi_u)$ state (high KER), capture to the

repulsive $H_2(b^3\Sigma_u^+)$ state (low KER), and NDC. Which state the electron is captured to can be determined once the Q-value measurement is completed (see chapters 3 and 7). Likely states to which the electron can be captured are the $H_2(c^3\Pi_u)$ state (which would result in a Q-value of about 12 eV for an argon target) and the H_2 $X^1\Sigma_g^+$ ground state (which would result in a Q-value of about 0 eV for an argon target).

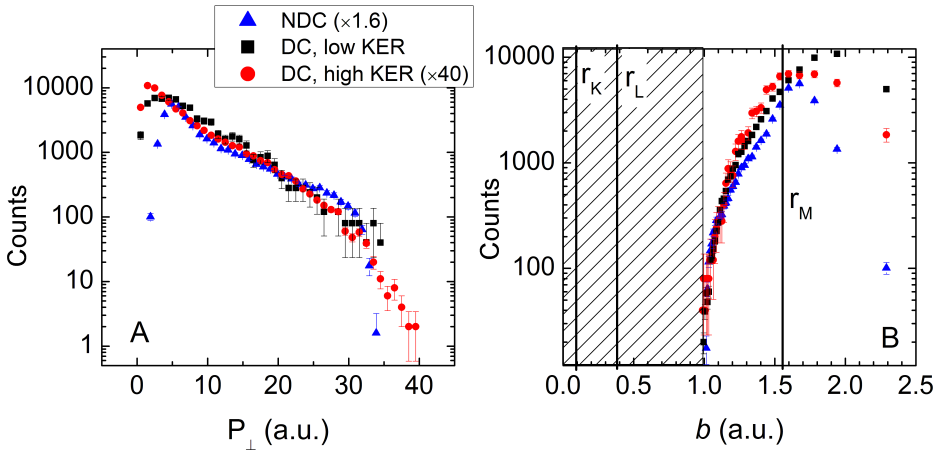

Figure 5.3: (A) Transverse momentum distribution for the recoil ions from the NDC and DC channels. Panel (B) is the conversion of $P_\perp$ to impact parameter, b, assuming an exponentially screened potential for argon. More details are included in the text. The weighted averages for the electronic shell radii for the argon atom are shown in (B) as vertical lines and the shaded area is the width of the L shell, defined approximately as the weighted average ± 3 standard deviations.

5.2 Non-Dissociative Target Ionization

Similar to NDC, non-dissociative target ionization (NDTI) is a difficult channel to measure with our setup, since there is no break-up energy to help clear the Faraday cup and reach the detector. Therefore, we are limited to measuring only the fraction of this reaction which undergoes a hard enough collision for the surviving H_2^+ to reach the detector. The transverse momentum distribution is shown in Fig. 5.4 where events distorted by (1) the Faraday cup and bar and (2) elongation of the jet in the y direction have been eliminated. This data, despite having a well resolved time-difference peak is also further cleaned from

random coincidences by imposing transverse momentum conservation.

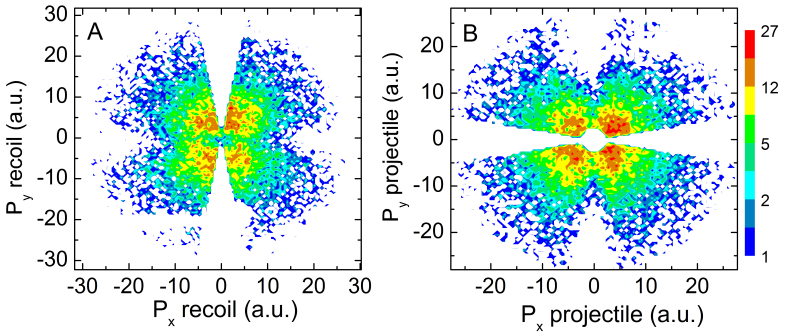

Figure 5.4: NDTI transverse momentum distributions for (A) the recoil ion and (B) the projectile after gating to exclude the distortions caused by the Faraday cup and its holding bar and the broadening caused by the jet velocity spread.

As the collision must be close, it is then surprising that the molecular ion remains bound. The possible mechanisms which lead to NDTI (Eq. 5.2) are:

(1) electron capture to autoionizing states:

$$H_2^+ + Ar \rightarrow H_2^{**} + Ar^+ \rightarrow H_2^+ + Ar^+ + e^- \tag{5.3}$$

(2) target excitation to autoionizing states:

$$H_2^+ + Ar \rightarrow H_2^+ + Ar^{**} \rightarrow H_2^+ + Ar^+ + e^- \tag{5.4}$$

and (3) direct target ionization

$$H_2^+ + Ar \rightarrow H_2^+ + Ar^+ + e^-. \tag{5.5}$$

Note that there is no electronic excitation of the projectile, since this would result in the dissociation of the H_2^+ (like in eCID). By comparing $P_\perp$ and b for NDTI and NDC, as shown in Fig. 5.5 we see the agreement between the two channels is good. Therefore, we can speculate that the most likely mechanism is Eq. 5.3, where the electron is first captured to H_2^{**} which then autoionizes. As mentioned earlier, direct target ionization (Eq. 5.5) is expected to be negligible at this collision velocity [41]. Q-values are expected to help determine the reaction mechanism leading to $H_2^+ + Ar^+ + e^-$.

Independent of the mechanism we can infer the projectile's alignment based on the findings of the counterpart channel where the molecular ion breaks (CID-TI), since the angular distribution, $\cos\theta$, cannot be measured for the non-dissociative processes. We know that in order to even be able to measure NDTI, it must undergo a close collision. Referring back to the ball-and-spring model proposed in chapter 4, if the molecule is aligned perpendicular to its motion, it will get vibrationally excited (like in vCID). If it is excited vibrationally enough, it will break. Therefore vibrational excitation has to be low. Hence, it is very likely that the molecules are aligned along their velocity in order to result in NDTI.

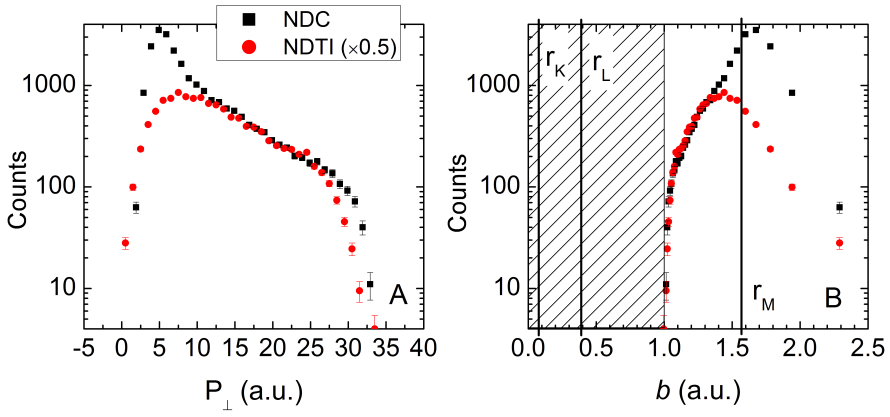

Figure 5.5: (A) Transverse momentum distribution for the recoil ions from the NDTI and NDC channels. We see that the NDC and NDTI are similar, thus hinting that maybe NDTI occurs by mechanism 5.3. Note that the distribution below about 4 a.u. is not well defined due to losses into the Faraday cup. (B) Impact parameter, b, distributions for NDTI and NDC assuming an exponentially screened Coulomb potential for argon (for more details see section 4.5). The weighted average for the electronic shell radius for the argon atom are shown in (B) as vertical lines, and the shaded area is the width of the L shell, defined approximately as the weighted average ± 3 standard deviations.

Chapter 6

Overall Comparison

Simultaneous measurement of all accessible reaction channels is one of the main advantages of the two experimental setups presented in this thesis. Therefore a direct comparison can be made for all reactions under identical experimental conditions.

6.1 "Cell" Channels Comparison

As an example of direct comparison of the various channels involved, we plot the projectile scattering angle, θ_{cm}, for DC and CID, broken into its two contributing mechanisms, namely eCID and vCID (discussed in chapter 4).

From the scattering angle distributions for DC, eCID and vCID, shown in Fig. 6.1, we can compare the different mechanisms[1]. We notice that, for 3 keV H_2^+ impinging on argon, CID and DC are nearly equal in magnitude, where vCID by itself is much less likely than eCID or DC. We also see that the θ_{cm} is small for eCID and DC and large for vCID. Since θ_{cm} is proportional to the transverse momentum, $P_\perp$, and therefore inversely proportional to the impact parameter, b, (see Eq. 4.5) we can also say that vCID occurs for small impact parameters where eCID and DC occur at larger impact parameters.

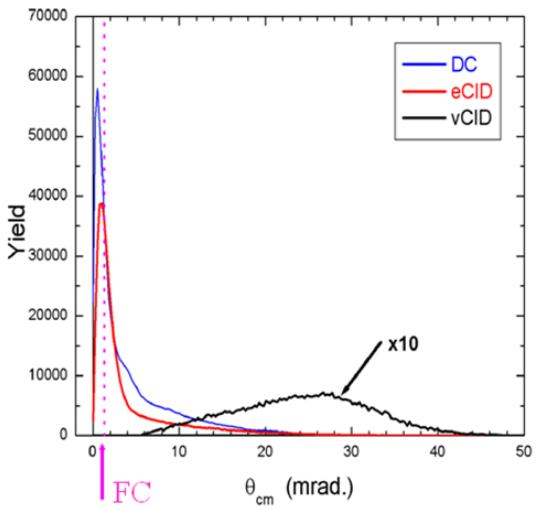

Figure 6.1: Comparison of scattering angle of the projectile center of mass for the channels measured with the target cell setup. Note that the center of mass of the projectile fragments typically falls within the Faraday cup (FC) radius for eCID and DC.

6.2 "Jet" Channels Comparison

Likewise for the "jet" setup, we compare $P_\perp$ and b for all channels[2]. The distributions for all channels are shown in Fig. 6.2, and again in Fig. 6.3 with the different mechanisms separated. For small $P_\perp$ the spectrum is dominated by DC and CID. Note that small $P_\perp$ is not measurable for NDC and NDTI, but likely NDC also extends to this region. If we break CID into eCID and vCID and DC into the "high" KER (capture to $c^3\Pi_u$) and "low" KER (capture to $b^3\Sigma_u^+$), we find that the spectrum is dominated by eCID and "low" KER DC.

In the middle of the $P_\perp$ distribution (between 10 and 30 a.u.), all channels seem to be monotonically decreasing. However, in Fig. 6.3, we see that vCID and vCID-TI are peaking in this range. In the large $P_\perp$ range (beyond 30 a.u.), we see that NDC, NDTI, "low" KER DC, vCID-TI and vCID are the main contributors.

Looking at Fig. 6.2, it appears that all channels extend to small b (on the order of

[1]Note that the losses due to detector efficiency and other experimental factors (such as losing a t_2 signal for DC or losing an event into the Faraday cup) are minor.

[2]Again, the losses due to detector efficiency are minor and the only notable experimental loss, different from that of the cell setup, is for the NDC and NDTI events which are lost into the Faraday cup.

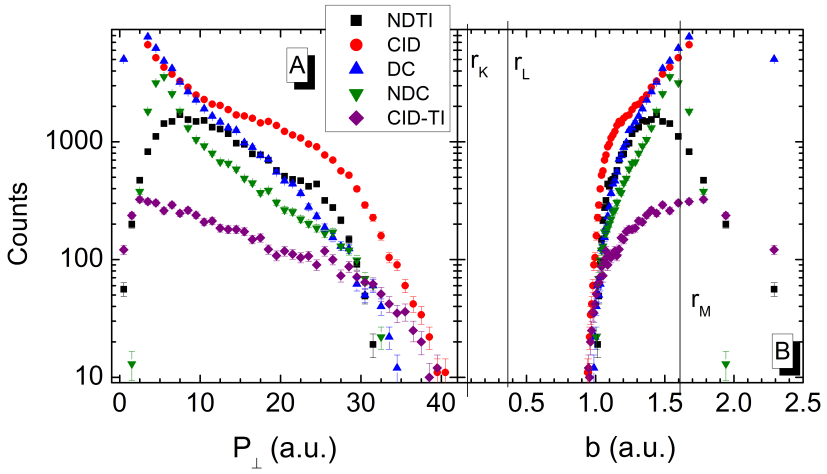

Figure 6.2: (A) Transverse momentum and (B) impact parameter, b, distributions for all reaction channels for 3 keV H_2^+ collisions with argon.

the size of target argon atom radius), where b is calculated by the exponentially screened Coulomb potential model as discussed in section 4.5. If we consider the average values of the radii of the electron shells (r_K, r_L, and r_M) [45], the collisions are surprisingly occurring well within the M shell of the argon atom. This is still the case when the individual mechanisms are considered, see Fig. 6.3. Better understanding of these findings requires a theoretical treatment of the collision process.

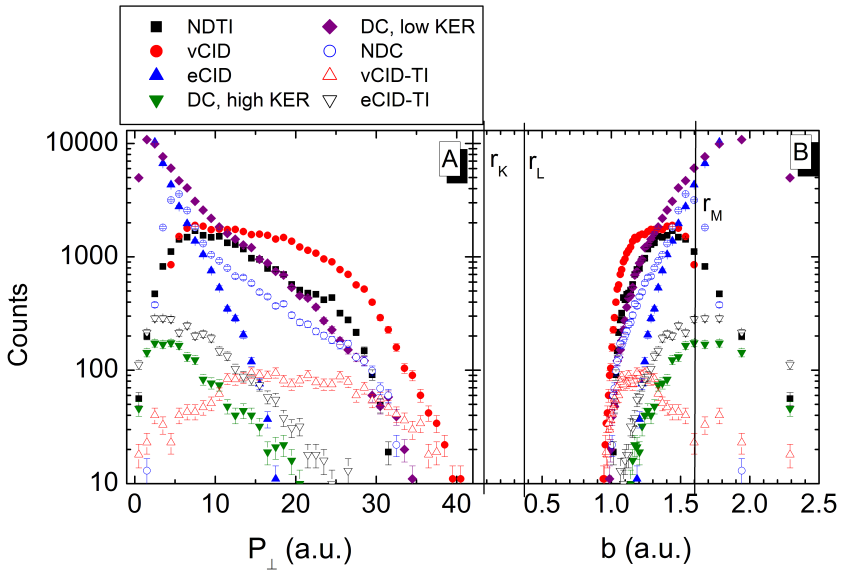

Figure 6.3: (A) Transverse momentum and (B) impact parameter, b, distributions for all channels for 3 keV H_2^+ collisions with argon, separated into their contributing mechanisms.

Chapter 7

Concluding Remarks and Future Directions

Presented in this thesis were (1) results from previous experiments using a target "cell" setup and (2) an experimental "jet" method for simultaneously measuring beam fragments and recoil ions. The latter method enables the study of DC and CID as well as their large-angle-scattering, non-dissociative counterparts, NDC and NDTI. First results from the developed "jet" method are presented. As this thesis is just one leg of a much larger project, a few of the many future directions of the project are discussed here also.

7.1 Concluding Remarks

Using the "cell" setup, we measure the molecular dissociation of simple diatomic molecular ions. We investigated dissociative capture (DC) – excluding the recoil ions, as discussed in chapter 3 – and collision induced dissociation (CID) – which can be further broken down into electronic (eCID) and vibrational (vCID) mechanisms – as discussed in chapter 4. Our results for DC and CID are in nice agreement with previous findings. Furthermore, we find that our eCID results agree nicely with theoretical predictions by Green and Peek [26]. Also, we describe eCID and vCID within a simple ball-and-spring model to explain the different angular dependencies. In addition, we compare the CID channel for H_2^+ and HeH^+ and find that at 1.5 keV/amu collisions, eCID is suppressed in HeH^+ and vCID is enhanced.

The innovative experimental method, with a longitudinal extraction field for molecular dissociation and recoil ion imaging, is described in chapter 2. This method can be extended for studies of polyatomic molecular ions impinging on noble gas targets, or even molecular targets.

The imaging equations for the recoiling ion are described, and although we still need to perform an experiment to calibrate the Q-value, they will be important for the future development of the project. We find reasonable agreement between the old and new CID and DC measurements, although the new method suffers from larger beam divergence. We also demonstrated that non-dissociating processes such as non-dissociative capture (NDC) and non-dissociative target ionization (NDTI) can be measured given the projectile is scattered by more than about 0.13 degrees ($\sim$4.4 mrad) for a 3 keV H_2^+ beam.

For NDTI, we provide evidence that in order for the molecular ion to survive the close encounter, it is likely aligned along its velocity. Also, the similarity of the transverse momentum distribution to that of NDC suggests that electron capture to an autoionizing state of H_2 is the responsible mechanism. Confirmation of this mechanism relies upon an accurate Q-value measurement.

In chapter 4 we also answered the intriguing question of target ionization for CID by observing CID-TI. The target ionization occurs mainly for extremely close collisions in which the projectile penetrates into the L shell of argon (within the exponentially screened Coulomb potential model). The angular distributions agree with CID, except we suspect that long range Coulomb interactions play a role in the $\cos\alpha$ distribution for vCID-TI.

7.2 Future Directions

First and foremost for the experiments at hand, we need to perform a Q-value calibration experiment and improve the experimental resolution of the longitudinal momentum of the recoil ion. This includes reducing the energy spread of the ion beam and improving the readout of the voltage supplied to the spectometer. An independent measurement of the

beam energy indicates the spread to be about 15 eV, full width half maximum. In order to achieve the desired resolution for the Q-value, the beam spread should be on the order of a few eV. In addition, the readout on the power supply for the spectrometer (both the main voltage,V_s and the focus voltage V_f) was inaccurate to nearly 2 volts. A test with SIMION confirmed that a one volt change to V_s (i.e. 2084 V to 2085 V) will change the time of flight of a recoiling argon ion by more than two ns, therefore leading to an uncertainty of more than 5 eV for the Q-value. Attempts to improve the voltage readout are currently underway.

The next leg of the overall project is to develop a source of ions that is pulsed into picosecond bunches[1]. This should be possible by shining a pulsed laser onto a neutral gas target. In this way, we can start the electronic recording time with a regularly spaced signal which is correlated with the measurement. The benefit then is that we can measure both t_1 and t_2, as opposed to $t_2 - t_1$, and therefore reduce the assumptions needed for the data analysis. The present analysis assumes that z_i is negligible and v_{0z} is the average beam velocity.

Another future possibility is to measure electrons, since autoionization of either excited projectiles or target ions has not been ruled out as a possible process leading to the observed channels. Electrons ejected by autoionization are mono-energetic, and can be very helpful in determining the states involved in a given reaction. For example, the reaction channel $H_2^+ + Ar \rightarrow H_2^+ + Ar^+$ might occur by electron capture into doubly excited states followed by autoionization of excited H_2, or the H_2^+ might doubly excite the argon which then autoionizes.

[1]The best current experimental timing resolution is about 25 ps.

Bibliography

[1] S. Datz, G. W. F. Drake, T. F. Gallagher, H. Kleinpoppen, and G. zu Putlitz, Rev. Mod. Phys. **71**, S223 (1999).

[2] H. Martínez and F. B. Yousif, Phys. Rev. A **69**, 062701 (2004).

[3] D. P. de Bruijn, J. Nueteboom, V. Sidis, and J. Los, Chem. Phys. **85**, 215 (1984).

[4] R. G. Cooks, *Collision Spectroscopy*, New York: Plenum Press, 1978.

[5] D. K. Gibson, J. Los, and J. Schopman, Physica **40**, 385 (1968).

[6] S. J. Anderson and J. B. Swan, Phys. Lett. **48A**, 435 (1974).

[7] D. K. Gibson and J. Los, Physica **35**, 258 (1967).

[8] S. J. Anderson, J. Chem. Phys. **60**, 3278 (1974).

[9] R. Caudano and J. M. Delfosse, J. Phys. B: Atomic, Molecular and Optical Physics **1**, 813 (1968).

[10] G. W. McClure, Phys. Rev. **140**, A769 (1965).

[11] B. Meierjohann and M. Vogler, J. Phys. B: Atomic, Molecular and Optical Physics **9**, 1801 (1976).

[12] G. W. McClure, Phys. Rev. **130**, 1852 (1963).

[13] N. V. Fedorenko, V. V. Afrosimov, R. N. Il'in, D. M. Kaminker, and Z. Eksperim, Soviet Phys. JETP **9**, 267 (1959).

[14] D. R. Sweetman, Proc. Roy. Soc. (London) **A256**, 416 (1960).

[15] C. F. Barnett, M. Rankin, and J. A. Ray, Proceedings of the Sixth International Conference on Ionization Phenomena in Gases (Paris, 1963) **I**, 63 (1963).

[16] D. P. de Bruijn, J. Nueteboom, and J. Los, Chem. Phys. **85**, 233 (1984).

[17] W. Wu, M. H. Prior, and H. Bräuning, Phys. Rev. A **57**, R5 (1998).

[18] M. Saito, T. Muneda, M. Mitani, K. Oguri, and Y. Haruyama, J. Phys. B: Atomic, Molecular and Optical Physics **36**, 699 (2003).

[19] L. Ph. H. Schmidt, S. Schössler, F. Afaneh, M. Schöffler, K. E. Stiebing, H. Schmidt-Böcking, and R. Dörner, Phys. Rev. Lett. **101**, 173202 (2008).

[20] J. H. Posthumus, B. Fabre, C. Cornaggia, N. de Ruette, and X. Urbain, Phys. Rev. Lett. **101**, 233004 (2008).

[21] Y. Suzuki, T. Kaneko, M. Tomita, and M. Sakisaka, J. Phys. Soc. of Japan **55**, 3037 (1986).

[22] C. McGrath, M. B. Shah, P. C. E. McCartney, and J. W. McConkey, Phys. Rev. A **64**, 062712 (2001).

[23] J. C. Brenot, H. Dunet, J. A. Fayeton, M. Barat, and M. Winter, Phys. Rev. Lett. **77**, 1246 (1996).

[24] J. A. Fayeton, M. Barat, J. C. Brenot, H. Dunet, Y. J. Picard, U. Saalmann, and R. Schmidt, Phys. Rev. A **57**, 1058 (1998).

[25] M. Vogler and W. Seibt, Z. Phys. **210**, 337 (1968).

[26] T. A. Green and J. M. Peek, Phys. Rev. **183**, 166 (1969).

[27] T. A. Green, Phys. Rev. A **1**, 1416 (1970).

[28] D. Hennecart and J. Pascale, Phys. Rev. A **71**, 012710 (2005).

[29] R. Ünal, *Energy and Charge State Dependences of Transfer Ionization to Single Capture Ratio for Fast Multiply Charge Ions on Helium*, PhD thesis, Kansas State University, 2001.

[30] A. M. Sayler, *Measurements of Ultrashort Intense Laser-induced Fragmentation of Simple Molecular Ions*, PhD thesis, Kansas State University, 2008.

[31] D. R. Lide, *CRC Handbook of Chemistry and Physics*, volume 86th Ed., Boca Raton: CRC Press, 2005-2006.

[32] E. E. Nikitin and S. Y. Umanskii, *Theory of Slow Atomic Collisions*, Berlin Heidelberg: Springer-Verlag, 1984.

[33] A. Bárány, H. Danared, H. Cederquist, P. Hvelplund, H. Knudsen, J. O. K. Pedersen, C. L. Cocke, L. N. Tunnell, W. Waggoner, and J. P. Giese, J. Phys. B: Atomic, Molecular and Optical Physics **19**, L427 (1986).

[34] T. Brabec, *Strong Field Laser Physics*, New York: Springer, 2008.

[35] S. Knoop, *Recoil Ion Momentum Spectroscopy on He^{2+}–Na Collisions*, Master's thesis, University of Groningen, 2001.

[36] D. Fischer, B. Feuerstein, R. Moshammer, J. R. C. López-Urrutia, I. Draganic, H. Lörch, A. N. Perumal, J. Ullrich, and R. D. DuBois, Hyperfine Interactions **146/147**, 117 (2003).

[37] J. Ullrich, R. Moshammer, A. Dorn, R. Dörner, L. Ph. H. Schmidt, and H. Schmidt-Böcking, Rep. Prog. Phys. **66**, 1463 (2003).

[38] H. D. Hagstrum and J. T. Tate, Phys. Rev. **59**, 354 (1941).

[39] R. M. Wood, Q. Zheng, A. K. Edwards, and M. A.Mangan, Rev. Sci. Instrum. **68**, 1382 (1997).

[40] T. A. Green, H. H. Michels, J. C. Browne, and M. M. Madsen, J. Chem. Phys. **61**, 5186 (1974).

[41] W. Wu, C. L. Cocke, J. P. Giese, F. Melchert, M. L. A. Raphaelian, and M. Stockli, Phys. Rev. Lett. **75**, 1054 (1995).

[42] R. D. DuBois, I. Ali, C. L. Cocke, C. R. Feeler, and R. E. Olson, Phys. Rev. A **62**, 060701 (2000).

[43] I. Ali, R. D. DuBois, C. L. Cocke, S. Hagmann, C. R. Feeler, and R. E. Olson, Phys. Rev. A **64**, 022712 (2001).

[44] E. Everhart, G. Stone, and R. J. Carbone, Phys. Rev. **99**, 1287 (1955).

[45] C. F. Fischer, *The Hartree-Fock method for atoms: a numerical approach*, New York: Wiley, 1977.

Appendix A

Electronics

The focus of this appendix is to describe the electronics associated with processing the delay line detector signals. Other electronic setups for the beam viewer, ion beam current monitor, and front end electronics, are detailed in Sayler's Ph.D. thesis [30], since the same detection methods were used for his work.

A schematic outline of the electronics for the detector signals is shown in Fig. A.1. First it is important to point out that there is no periodic pulse synchronized to the measurement to provide a natural start (or stop) signal. Therefore, we trigger the electronics and set the time window by the first hit on the detector. The timing signal associated with the first hit comes from the front microchannel plate (MCP 'F') due to its better quality over the signal from the back plate (MCP 'B'). Coupling boxes are used for matching the impedance and for filtering. This timing signal is amplified using an Ortec VT120B pre-amp and is sent to a constant fraction discriminator (CFD) which produces a fast NIM pulse. An output from the CFD is delayed and used as a trigger for the time-to-digital converter (TDC). The delay of the trigger by the gate-and-delay generator determines the size of the time window for which events are recorded. The size of the window typically depends on the target gas. For argon, typical times of flight are about 10μs with a spectrometer voltage of about 2 kV. Two more signals, identical to the trigger signal (except they are not delayed), are sent to channels 0 and 5 of the TDC, where the difference in the cable length between these two outputs provides a short delay between the two signals. This delay is the t_1 constant offset.

Time difference is measured with respect to t_1 rather than the trigger signal as it has less jitter.

In addition to timing information from the MCP, we also record the position signals from the delay line anode. Wires labelled 'S' and 'D' stand for signal and difference, respectively. The signal wire voltage is 60 V higher than the voltage applied to the difference wire (typically 1900 V) in order to attract more electrons, which were generated by the MCP. Due to the proximity, each set of wires picks up similar amounts of noise and so, when the 'D' wire is subtracted from the 'S' wire, we get a pulse with better signal to noise ratio. Signals are differentially amplified and then sent to CFDs to generate fast NIM signals. One output from each CFD goes into a TDC and one goes into a scalar for recording the rates on all of the wires. More information on delay line detectors can be found on the RoentDek webpage (http://www.roentdek.com/).

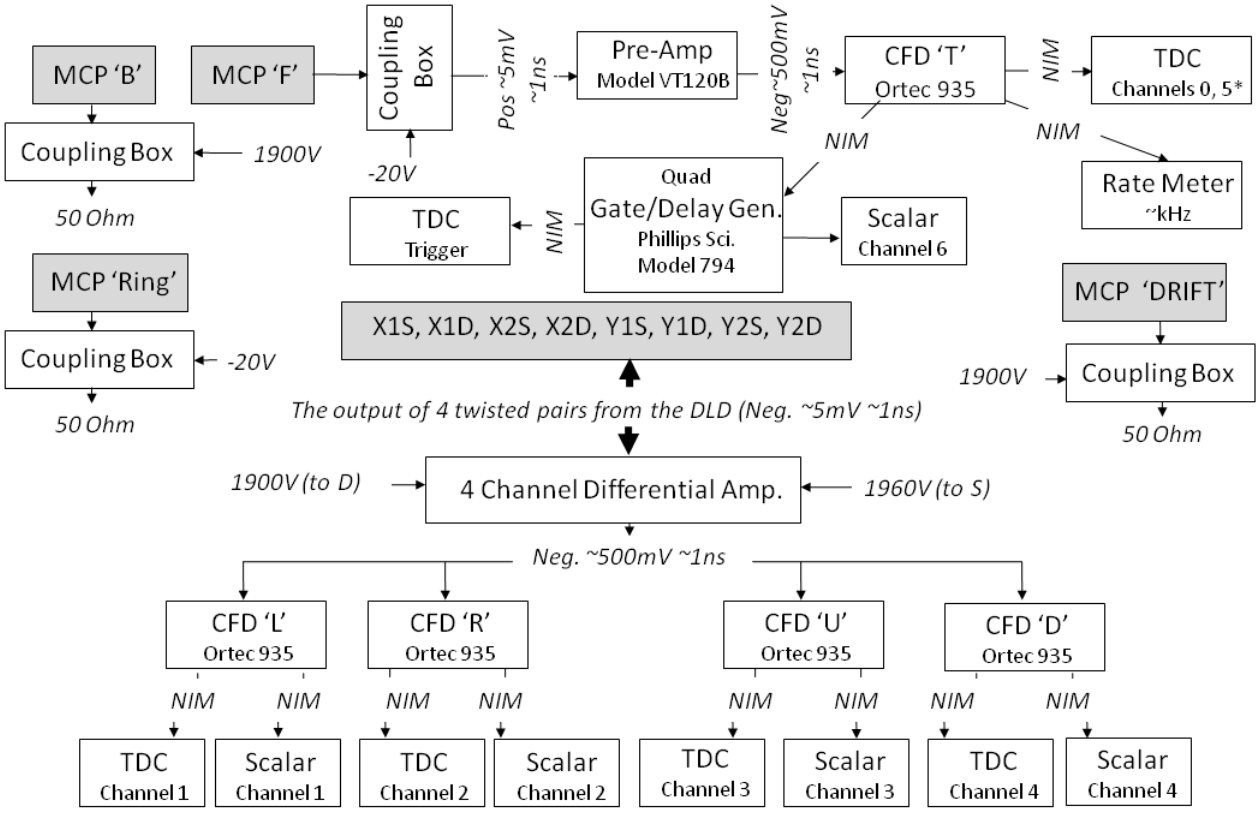

Figure A.1: Schematic of the electronics used. The cable connecting to channel 5 of the TDC must be longer than for channel 0 – the length difference between these two wires will determine the t_1 constant offset. Note that 'L', 'R', 'U', 'D', and 'T' are for left, right, up, down and time signals.

Appendix B

Imaging Recoil Longitudinal Velocity

B.1 Non-Dissociating Collisions

In this section we address non-dissociating collisions between a molecular ion AB^+ and a target atom. Note that this is identical to ion-atom collisions for which the recoil ion is extracted longitudinally.

B.1.1 Neutral–Ion (NDC)

Following electron capture, the projectile is neutralized and the target is ionized, therefore the time-of-flight (TOF) equations for this case are:

$$t_n = \frac{l_1\,(1 - z_i') + l_2 + l_3}{v_{0z}\,(1 + u_{nz})}, \tag{B.1}$$

and

$$\begin{aligned} t_r &= \tau_{1r}\left[\sqrt{u_{rz}^2 + \eta_1'} - u_{rz}\right] + \gamma\tau_{1r}\left[\sqrt{u_{rz}^2 + \eta_1' + \eta_2'} - \sqrt{u_{rz}^2 + \eta_1'}\right] \\ &\quad + \frac{l_3}{v_{0z}}\frac{1}{\sqrt{u_{rz}^2 + \eta_1' + \eta_2'}}, \end{aligned} \tag{B.2}$$

where $z_i' = z_i/l_1 \ll 1$, v_{0z} is the projectile velocity and v_{jz} the change in the projectile velocity in the z-direction which can be written $v_{0z} + v_{jz} = v_{0z}(1 + u_{jz})$, where $u_{jz} = \frac{v_{jz}}{v_{0z}}$ and subscript j denotes a recoil ion (r), charged projectile (p) or neutral projectile (n) quantity. Also,

$$\eta_i' = q_r V_i / \left(\frac{1}{2} M_r v_{0z}^2\right), \tag{B.3}$$

where subscript $i = 1$ denotes the first and $i = 2$, the second field regions of the focusing spectrometer (see section 2.2) and

$$\tau_{1r} \equiv \frac{M_r v_{0z} l_1 F}{q_r V_1}. \tag{B.4}$$

Note that due to 3D focusing of the recoil ions, it is not necessary to include the z_i' offset in t_r. All other variable definitions can be found in Table C.1.

Momentum conservation in the z-direction provides an additional equation

$$M_r v_{rz} + M_p \left(v_{0z} + v_{nz}\right) = M_p v_{0z}, \tag{B.5}$$

where v_{nz} is the additional velocity gained by the projectile from the collision and v_{0z} is its average initial velocity. Eq. B.5 reduces to $M_r v_{rz} + M_p v_{nz} = 0$, or to a similar relationship between the scaled velocities $M_r u_{rz} + M_p u_{nz} = 0$ upon division by v_{0z}. From this we can derive $u_{nz} = -\frac{M_r}{M_p} u_{rz} = -\beta_{rp} u_{rz}$, where we used the common definition of the mass ratio, namely $\beta_{rp} \equiv \frac{M_r}{M_p}$.

Now, substituting u_{nz} in Eq. B.1 and subtracting it from Eq. B.2, we get

$$\begin{aligned} T_{rn} \;=\; & t_r - t_n = \tau_{1r}\left[\sqrt{u_{rz}^2 + \eta_1'} - u_{rz}\right] + \gamma\tau_{1r}\left[\sqrt{u_{rz}^2 + \eta_1' + \eta_2'} - \sqrt{u_{rz}^2 + \eta_1'}\right] \\ & + \frac{l_3}{v_{0z}} \frac{1}{\sqrt{u_{rz}^2 + \eta_1' + \eta_2'}} - \frac{l_1\left(1 - z_i'\right) + l_2 + l_3}{v_{0z}\left(1 - \beta_{rp} u_{rz}\right)}, \end{aligned} \tag{B.6}$$

which can be solved numerically (without further approximations) for u_{rz}.

Once u_{rz} is evaluated we can determine the longitudinal momentum transfer to the recoil ion to be

$$P_{\parallel} = M_r u_{rz} v_{0z} \tag{B.7}$$

(in a.u.) and finally evaluate the reaction Q-value using the equations listed in subsection B.3.

First order solutions – To get a better feel for this problem, we can solve it approximately using linear expansions. Eq. B.1, in the linear approximation, reduces to

$$t_n \simeq t_{n0}\left\{1 - u_{nz}\right\}, \tag{B.8}$$

where

$$t_{n0} \equiv \frac{l_1\,(1-z_i') + l_2 + l_3}{v_{0z}}. \tag{B.9}$$

and Eq. B.2, in the linear approximation, reduces to

$$t_r \simeq t_{r0} - u_{rz}\tau_{1r}\,, \tag{B.10}$$

where we defined the TOF of a recoil "born" at rest (i.e. $u_{rz} = 0$) to be

$$t_{r0} \equiv \left[\tau_{1r}\sqrt{\eta_1'} + \gamma\tau_{1r}\left(\sqrt{\eta_1'+\eta_2'} - \sqrt{\eta_1'}\right) + \frac{l_3}{v_{0z}}\frac{1}{\sqrt{\eta_1'+\eta_2'}}\right]. \tag{B.11}$$

Now we use Eqs. B.8 and B.10, for the TOF instead of Eqs. B.1 and B.2. Substituting $u_{nz} = -\beta_{rp}u_{rz}$ in Eq. B.8 and subtracting it from Eq. B.10 yields

$$T_{rn} \simeq t_r - t_n \simeq (t_{r0} - u_{rz}\tau_{1r}) - t_{n0}\,(1+\beta_{rp}u_{rz})\,. \tag{B.12}$$

The equation above can be solved for u_{rz} yielding

$$u_{rz} \simeq \frac{(t_{r0}-t_{n0}) - T_{rn}}{\tau_{1r} + t_{n0}\beta_{rp}}\,. \tag{B.13}$$

As stated earlier, once u_{rz} is evaluated we can determine the longitudinal momentum transfer to the recoil ion, $P_\parallel$, and from it the reaction Q-value using the equations listed in sub-section B.3.

B.1.2 Ion–Ion (NDTI)

For non-dissociative target ionization (NDTI), the reaction products consist of an ionized target and the molecular ion. In this case, the TOF equations are:

$$\begin{aligned} t_p \;=\; & -(1+u_{pz})\,\tau_1 + \tau_1\,(1-\gamma)\sqrt{(1+u_{pz})^2 + \eta_1\,(1-z_i')} \\ & +\gamma\tau_1\sqrt{(1+u_{pz})^2 + \eta_1\,(1-z_i') + \eta_2} + \frac{l_3}{v_{0z}}\frac{1}{\sqrt{(1+u_{pz})^2 + \eta_1\,(1-z_i') + \eta_2}}, \end{aligned} \tag{B.14}$$

where

$$\tau_1 = \frac{M_p v_{0z} l_1 F}{q_p V_1}, \tag{B.15}$$

and we use Eq. B.2 for the recoil ion flight time.

Momentum conservation in the z-direction provides an additional equation

$$M_r v_{rz} + M_p \left(v_{0z} + v_{pz}\right) = M_p v_{0z}\,, \tag{B.16}$$

where v_{pz} is the additional velocity gained by the projectile from the collision. Eq. B.16 reduces to $M_r v_{rz} + M_p v_{pz} = 0$, or to a similar relationship between the scaled velocities $M_r u_{rz} + M_p u_{pz} = 0$ upon division by v_{0z}. From this we can derive $u_{pz} = -\frac{M_r}{M_p} u_{rz} = -\beta_{rp} u_{rz}$.

Now, substituting $u_{pz} = -\beta_{rp} u_{rz}$ in Eq. B.14 and subtracting it from Eq. B.2, we get the equation

$$\begin{aligned} T_{rp} = t_r - t_p = \tau_{1r}\left[\sqrt{u_{rz}^2 + \eta_1'} - u_{rz}\right] + \gamma\tau_{1r}\left[\sqrt{u_{rz}^2 + \eta_1' + \eta_2'} - \sqrt{u_{rz}^2 + \eta_1'}\right] \\ + \frac{l_3}{v_{0z}} \frac{1}{\sqrt{u_{rz}^2 + \eta_1' + \eta_2'}} + (1 - \beta_{rp} u_{rz})\tau_1 - \tau_1 (1-\gamma)\sqrt{(1-\beta_{rp}u_{rz})^2 + \eta_1 (1 - z_i')} \\ -\gamma\tau_1\sqrt{(1-\beta_{rp}u_{rz})^2 + \eta_1 (1-z_i') + \eta_2} - \frac{l_3}{v_{0z}} \frac{1}{\sqrt{(1-\beta_{rp}u_{rz})^2 + \eta_1 (1-z_i') + \eta_2}}\,, \end{aligned} \tag{B.17}$$

which can be solved numerically for u_{rz} without further approximations.

Once u_{rz} is evaluated we can determine the longitudinal momentum transfer to the recoil ion, $P_{\|}$, and from it the reaction Q-value using the equations listed in sub-section B.3.

First order solutions – To get a better feel for this problem, we can solve it approximately using linear expansions. In first order, Eq. B.14 reduces to

$$t_p \simeq t_{p0} - u_{pz}\tau_p \tag{B.18}$$

where $t_{p0} \equiv -\tau_1 + \tau_1 (1-\gamma)\sqrt{1 + \eta_1 (1 - z_i')} + \gamma\tau_1\sqrt{1 + \eta_1 (1-z_i') + \eta_2} + \frac{l_3}{v_{0z}} \frac{1}{\sqrt{1+\eta_1\left(1-z_i'\right)+\eta_2}}$, and $\tau_p \equiv \tau_1 - \frac{\tau_1(1-\gamma)}{\sqrt{1+\eta_1\left(1-z_i'\right)}} - \frac{\gamma\tau_1}{\sqrt{1+\eta_1\left(1-z_i'\right)+\eta_2}} + \frac{l_3}{v_{0z}} \frac{1}{\left[1+\eta_1\left(1-z_i'\right)+\eta_2\right]^{3/2}}$ and Eq. B.2 reduces to Eq. B.10.

Now we use Eqs. B.18 and B.10 for the TOF instead of Eqs. B.14 and B.2. Substituting $u_{pz} = -\beta_{rp} u_{rz}$ in Eq. B.18 and subtracting it from Eq. B.10 yields

$$T_{rp} \simeq t_r - t_p \simeq (t_{r0} - u_{rz}\tau_{1r}) - (t_{p0} + \beta_{rp} u_{rz}\tau_p)\,. \tag{B.19}$$

The equation above can be solved for u_{rz}, yielding:

$$u_{rz} \simeq \frac{(t_{r0} - t_{p0}) - T_{rp}}{\tau_{1r} + \beta_{rp}\tau_p}. \tag{B.20}$$

Again, once u_{rz} is evaluated we can determine the longitudinal momentum transfer to the recoil ion, $P_{\|}$, and from it the reaction Q-value using the equations listed in sub-section B.3.

B.2 Dissociating Collisions

In this section we address dissociating collisions between a molecular ion AB^+ and a target atom. Note that both beam fragments and the recoil ion are extracted longitudinally.

The approach for solving this longitudinal imaging problem is based on viewing the collision as a two step process. First, the molecular ion collides with the atom leading to electron capture or excitation of either the projectile or the target. Second the molecular ion dissociates. Therefore we can write momentum conservation conditions for each case, specifically

$$M_r v_{rz} + M_p \left(v_{0z} + v_{cmz}\right) = M_p v_{0z}, \tag{B.21}$$

for the first step, which is similar to Eqs. B.5 and B.16 used earlier. Note that here we denote the longitudinal velocity change of the projectile by v_{cmz} instead of v_{nz} and v_{pz} used previously for the nondissociating reactions. For the second step – the dissociation of the molecule – we use the momentum conservation in the post collision center-of-mass (CM) frame, namely

$$m_1 v'_{1z} + m_2 v'_{2z} = 0, \tag{B.22}$$

where v'_{1z} and v'_{2z} are the velocities of the two beam fragments in the post collision projectile CM frame (1 and 2 indicating order of hits on the detector), and m_1 and m_2 are the masses of the two fragments ($m_1 + m_2 = M_p$). For convenience, the momentum conservation equations above can be written in terms of the scaled velocities, $u_{jz} = v_{jz}/v_{0z}$ and $u'_{jz} = v'_{jz}/v_{0z}$, explicitly yielding

$$u_{cmz} = -\frac{M_r}{M_p} u_{rz} = -\beta_{rp} u_{rz} \tag{B.23}$$

$$u'_{2z} = -\frac{m_1}{m_2} u'_{1z} = -\beta_{12} u'_{1z}. \tag{B.24}$$

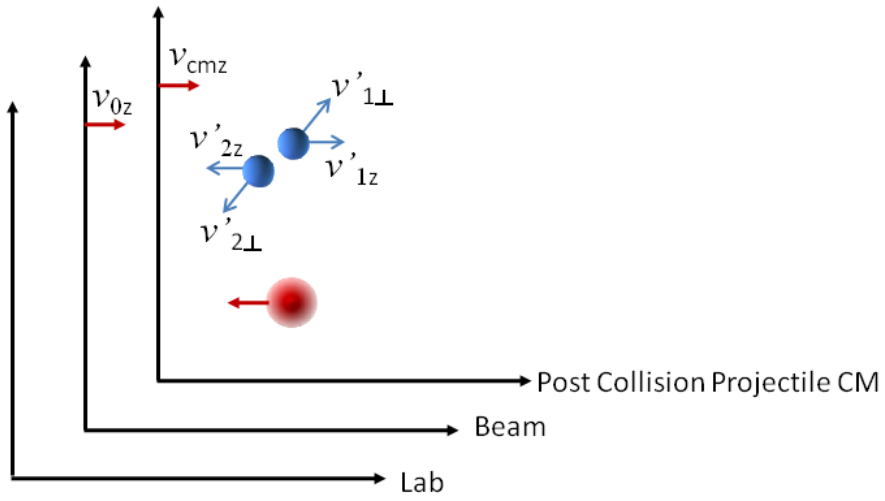

Figure B.1: Schematic of the reference frames used to describe the collisions.

With this picture in mind, the longitudinal velocities of the three particles in the lab frame are given by

$$\begin{aligned} v_{1z} &= v_{0z} + v_{cmz} + v'_{1z} = v_{0z}\left(1 + u_{cmz} + u'_{1z}\right) \\ v_{2z} &= v_{0z} + v_{cmz} + v'_{2z} = v_{0z}\left(1 + u_{cmz} + u'_{2z}\right) \\ v_{rz} &= v_{0z} u_{rz}. \end{aligned} \tag{B.25}$$

The velocity of the post collision projectile CM reference frame, used above to describe the molecular dissociation, can be defined as

$$v'_{0z} \equiv v_{0z} + v_{cmz}. \tag{B.26}$$

It is convenient to also define the scaled dissociation velocities, v'_{jz}, with respect to the v'_{0z} velocity, namely $u''_{jz} = v'_{jz}/v'_{0z}$ (where $j = 1, 2$) as it will simplify the calculation of the

dissociation velocities in the post-collision CM frame. This new scaled velocity u''_{jz} is very close in magnitude to the other scaled velocity u'_{jz} as they are related by

$$u''_{jz} = u'_{jz}\frac{1}{1+u_{cmz}}, \tag{B.27}$$

and typically $u_{cmz} \ll 1$.

B.2.1 Neutral–Neutral–Ion (DC)

In this case we have two neutral beam fragments followed by a recoil ion. The TOFs of these particles for this specific case can be written as

$$t_1 = t_{n_1} = \frac{l_1\,(1-z'_i)+l_2+l_3}{v_{0z}\,(1+u_{cmz}+u'_{1z})} = \frac{l_1\,(1-z'_i)+l_2+l_3}{v'_{0z}\,(1+u''_{1z})}, \tag{B.28}$$

and

$$t_2 = t_{n_2} = \frac{l_1\,(1-z'_i)+l_2+l_3}{v_{0z}\,(1+u_{cmz}+u'_{2z})} = \frac{l_1\,(1-z'_i)+l_2+l_3}{v'_{0z}\,(1+u''_{2z})}, \tag{B.29}$$

respectively, for the first and second fragments. The flight time for the recoil ion is the same as for the non-dissociating cases, i.e. Eq. B.2. We have used this concept of imaging in the post-collision CM frame (see Fig. B.1) previously in our molecular dissociation imaging technique as this is the frame of reference in which Eq. B.22 is valid. Furthermore, the solution of the equation resulting from the subtraction of Eq. B.29 from Eq. B.28 for u''_{1z} is already implemented in our analysis for the projectiles – all that we need to change is the value for v'_{0z}. Moreover, when we symmetrize the u''_{1z} (or v'_{1z}) distribution of the dissociating fragments, the beam velocity that we are determining is the post-collision projectile CM velocity, v'_{0z}.

A more general approach would be to write the T_{21} and T_{r1} time differences using the projectile velocity before the collision, v_{0z},

$$T_{21} \equiv t_2 - t_1 = \frac{l_1\,(1-z'_i)+l_2+l_3}{v_{0z}\,(1+u_{cmz}+u'_{2z})} - \frac{l_1\,(1-z'_i)+l_2+l_3}{v_{0z}\,(1+u_{cmz}+u'_{1z})}, \tag{B.30}$$

and

$$T_{r1} \equiv t_r - t_1 = \tau_{1r}\left[\sqrt{u_{rz}^2+\eta_1'} - u_{rz}\right] + \gamma\tau_{1r}\left[\sqrt{u_{rz}^2+\eta_1'+\eta_2'} - \sqrt{u_{rz}^2+\eta_1'}\right] + \frac{l_3}{v_{0z}}\frac{1}{\sqrt{u_{rz}^2+\eta_1'+\eta_2'}} - \frac{l_1\left(1-z_i'\right)+l_2+l_3}{v_{0z}\left(1+u_{cmz}+u_{1z}'\right)}. \tag{B.31}$$

Substituting $u_{cmz} = -\beta_{rp}u_{rz}$ and $u_{2z}' = -\beta_{12}u_{1z}'$ from momentum conservation yields

$$T_{21} \equiv t_2 - t_1 = \frac{l_1\left(1-z_i'\right)+l_2+l_3}{v_{0z}\left(1-\beta_{rp}u_{rz}-\beta_{12}u_{1z}'\right)} - \frac{l_1\left(1-z_i'\right)+l_2+l_3}{v_{0z}\left(1-\beta_{rp}u_{rz}+u_{1z}'\right)}, \tag{B.32}$$

and

$$T_{r1} \equiv t_r - t_1 = \tau_{1r}\left[\sqrt{u_{rz}^2+\eta_1'} - u_{rz}\right] + \gamma\tau_{1r}\left[\sqrt{u_{rz}^2+\eta_1'+\eta_2'} - \sqrt{u_{rz}^2+\eta_1'}\right] + \frac{l_3}{v_{0z}}\frac{1}{\sqrt{u_{rz}^2+\eta_1'+\eta_2'}} - \frac{l_1\left(1-z_i'\right)+l_2+l_3}{v_{0z}\left(1-\beta_{rp}u_{rz}+u_{1z}'\right)}. \tag{B.33}$$

These coupled equations can be solved numerically.

Now u_{1z}' and u_{rz} can be evaluated, using the average beam velocity, v_{0z}, from an independent measurement, for example, using the beam-energy analyzer. To improve this situation in the future and evaluate v_{0zi}, the pre-collision velocity of each individual molecular ion, we need a pulsed (sub ns) molecular-ion beam that will enable the direct measurement of all the required TOF values above.

First order solutions – As for the nondissociating reactions, in order to get a better feel for this problem we can first solve the problem approximately using linear expansions:

$$t_1 = t_n \simeq t_{n0}\left(1-u_{1z}\right) = t_{n0}\left(1-\left[u_{cmz}+u_{1z}'\right]\right), \tag{B.34}$$

$$t_2 = t_n \simeq t_{n0}\left(1-u_{2z}\right) = t_{n0}\left(1-\left[u_{cmz}+u_{2z}'\right]\right). \tag{B.35}$$

The first order approximation for the recoil ion TOF is given by Eq. B.10. We substitute $u_{cmz} = -\beta_{rp}u_{rz}$ and $u_{2z}' = -\beta_{12}u_{1z}'$ from momentum conservation and rewrite in terms of time difference:

$$T_{21} = t_2 - t_1 \simeq t_{n0}\left(1+\beta_{rp}u_{rz}+\beta_{12}u_{1z}'\right) - t_{n0}\left(1+\beta_{rp}u_{rz}-u_{1z}'\right), \tag{B.36}$$

$$T_{r1} = t_r - t_1 \simeq t_{r0} - u_{rz}\tau_{1r} - t_{n0}\left(1+\beta_{rp}u_{rz}-u_{1z}'\right). \tag{B.37}$$

The dissociation velocity is determined from Eq. B.36 to be

$$u'_{1z} \simeq \frac{T_{21}}{t_{n0}\left[\beta_{12}+1\right]}. \tag{B.38}$$

The recoil velocity is evaluated from Eq. B.37 after substitution of the solution for u'_{1z}, explicitly: $T_{r1} \simeq t_{r0} - u_{rz}\tau_{1r} - t_{n0}\left(1+\beta_{rp}u_{rz}-u'_{1z}\right) = t_{r0} - u_{rz}\tau_{1r} - t_{n0}\left(1+\beta_{rp}u_{rz}-\frac{T_{21}}{t_{n0}[\beta_{12}+1]}\right)$ $= t_{r0} - u_{rz}\tau_{1r} - t_{n0} - t_{n0}\beta_{rp}u_{rz} + \frac{T_{21}}{[\beta_{12}+1]} = t_{r0} - t_{n0} + \frac{T_{21}}{[\beta_{12}+1]} - \left(\tau_{1r}+t_{n0}\beta_{rp}\right)u_{rz}$, which leads to $\left(\tau_{1r}+t_{n0}\beta_{rp}\right)u_{rz} \simeq t_{r0} - t_{n0} + \frac{T_{21}}{[\beta_{12}+1]} - T_{r1}$, and finally the expression for u_{rz}:

$$u_{rz} \simeq \frac{t_{r0} - t_{n0} + \frac{T_{21}}{\beta_{12}+1} - T_{r1}}{\tau_{1r}+t_{n0}\beta_{rp}}. \tag{B.39}$$

Again, once u_{rz} is evaluated we can determine the longitudinal momentum transfer to the recoil ion, $P_{\|}$, and from it the reaction Q-value using the equations listed in sub-section B.3.

B.2.2 Ion–neutral–Ion (CID-TI)

In this case we have one charged and one neutral beam fragment (in this time order because of the spectrometer field) followed by a recoil ion, and the TOF of these particles can be written for this specific case respectively as

$$\begin{aligned} t_1 \;=\; t_{p1} = &-\left(1+u_{cmz}+u'_{1z}\right)\tau_1 + \tau_1\left(1-\gamma\right)\sqrt{\left(1+u_{cmz}+u'_{1z}\right)^2+\eta_1\left(1-z'_i\right)} \\ &+\gamma\tau_1\sqrt{\left(1+u_{cmz}+u'_{1z}\right)^2+\eta_1\left(1-z'_i\right)+\eta_2} + \frac{l_3}{v_{0z}}\frac{1}{\sqrt{\left(1+u_{cmz}+u'_{1z}\right)^2+\eta_1\left(1-z'_i\right)+\eta_2}}, \end{aligned} \tag{B.40}$$

$$t_2 = t_{n_2} = \frac{l_1\left(1-z'_i\right)+l_2+l_3}{v_{0z}\left(1+u_{cmz}+u'_{2z}\right)} \tag{B.41}$$

and t_r again is given by Eq. B.2 and we used $u_{pz} \equiv u_{cmz}+u'_{1z}$ and $u_{nz} \equiv u_{cmz}+u'_{2z}$ in Eqs. B.40 and B.41, respectively.

In this case we adopt only the general approach suggested in the previous sub-section B.2.1. We therefore write the T_{21} and T_{r2} (we use the difference between the recoil and neutral fragment TOF for simplicity) time differences using the projectile velocity before

the collision, v_{0z},

$$\begin{aligned} T_{21} \equiv\ & t_2 - t_1 = \frac{l_1\left(1-z_i'\right)+l_2+l_3}{v_{0z}\left(1+u_{cmz}+u_{2z}'\right)} + \left(1+u_{cmz}+u_{1z}'\right)\tau_1 \\ & -\tau_1\left(1-\gamma\right)\sqrt{\left(1+u_{cmz}+u_{1z}'\right)^2+\eta_1\left(1-z_i'\right)} \\ & -\gamma\tau_1\sqrt{\left(1+u_{cmz}+u_{1z}'\right)^2+\eta_1\left(1-z_i'\right)+\eta_2} \\ & -\frac{l_3}{v_{0z}}\frac{1}{\sqrt{\left(1+u_{cmz}+u_{1z}'\right)^2+\eta_1\left(1-z_i'\right)+\eta_2}} \end{aligned} \tag{B.42}$$

$$\begin{aligned} T_{r2} \equiv\ & t_r - t_2 = \tau_{1r}\left[\sqrt{u_{rz}^2+\eta_1'}-u_{rz}\right] + \gamma\tau_{1r}\left[\sqrt{u_{rz}^2+\eta_1'+\eta_2'}-\sqrt{u_{rz}^2+\eta_1'}\right] \\ & +\frac{l_3}{v_{0z}}\frac{1}{\sqrt{u_{rz}^2+\eta_1'+\eta_2'}} - \frac{l_1\left(1-z_i'\right)+l_2+l_3}{v_{0z}\left(1+u_{cmz}+u_{2z}'\right)}. \end{aligned} \tag{B.43}$$

Substituting $u_{cmz} = -\beta_{rp}u_{rz}$ and $u_{2z}' = -\beta_{12}u_{1z}'$ from momentum conservation yields:

$$\begin{aligned} T_{21} =\ & \frac{l_1\left(1-z_i'\right)+l_2+l_3}{v_{0z}\left(1-\beta_{rp}u_{rz}-\beta_{12}u_{1z}'\right)} + \left(1-\beta_{rp}u_{rz}+u_{1z}'\right)\tau_1 \\ & -\tau_1\left(1-\gamma\right)\sqrt{\left(1-\beta_{rp}u_{rz}+u_{1z}'\right)^2+\eta_1\left(1-z_i'\right)} \\ & -\gamma\tau_1\sqrt{\left(1-\beta_{rp}u_{rz}+u_{1z}'\right)^2+\eta_1\left(1-z_i'\right)+\eta_2} \\ & -\frac{l_3}{v_{0z}}\frac{1}{\sqrt{\left(1-\beta_{rp}u_{rz}+u_{1z}'\right)^2+\eta_1\left(1-z_i'\right)+\eta_2}}, \end{aligned} \tag{B.44}$$

and

$$\begin{aligned} T_{r2} =\ & \tau_{1r}\left[\sqrt{u_{rz}^2+\eta_1'}-u_{rz}\right] + \gamma\tau_{1r}\left[\sqrt{u_{rz}^2+\eta_1'+\eta_2'}-\sqrt{u_{rz}^2+\eta_1'}\right] \\ & +\frac{l_3}{v_{0z}}\frac{1}{\sqrt{u_{rz}^2+\eta_1'+\eta_2'}} - \frac{l_1\left(1-z_i'\right)+l_2+l_3}{v_{0z}\left(1-\beta_{rp}u_{rz}-\beta_{12}u_{1z}'\right)}. \end{aligned} \tag{B.45}$$

These coupled equations can be solved numerically. Note that in this choice the v_{1z}' distribution is also symmetric about zero, as discussed in sub-section B.2.1.

First order solutions – As for the non-dissociating reactions, in order to get a better feel for this problem we can first solve the problem approximately using linear expansions. For the charged fragment, we find

$$t_1 = t_p \simeq t_{p0} - \tau_p u_{pz} \simeq t_{p0} - \tau_p\left(u_{cmz}+u_{1z}'\right). \tag{B.46}$$

The neutral fragment, t_2, and recoil ion, t_r, expansions are given by Eqs. B.35 and B.10, respectively.

We now use Eqs. B.46, B.35 and B.10, for the TOF instead of Eqs. B.40, B.29, and B.2. In this case $u_{pz} \equiv u_{cmz} + u'_{1z}$ and $u_{nz} \equiv u_{cmz} + u'_{2z}$. We substitute $u_{cmz} = -\beta_{rp} u_{rz}$ and $u'_{2z} = -\beta_{12} u'_{1z}$ from momentum conservation and write the time-difference equations:

$$T_{21} = t_2 - t_1 \simeq t_{n0}\left(1 + \beta_{rp} u_{rz} + \beta_{12} u'_{1z}\right) - t_{p0} + \tau_p\left(-\beta_{rp} u_{rz} + u'_{1z}\right), \tag{B.47}$$

$$T_{r2} = t_r - t_1 \simeq t_{r0} - u_{rz}\tau_{1r} - t_{n0}\left(1 + \beta_{rp} u_{rz} + \beta_{12} u'_{1z}\right). \tag{B.48}$$

Eq. B.48 can be simplified to

$$T_{r2} \simeq t_{r0} - t_{n0} - u_{rz}\left(t_{n0}\beta_{rp} + \tau_{1r}\right) - u'_{1z} t_{n0}\beta_{12}. \tag{B.49}$$

By solving Eq. B.49 for u'_{1z} we get:

$$u'_{1z} \simeq \frac{t_{r0} - t_{n0} - u_{rz}\left(t_{n0}\beta_{rp} + \tau_{1r}\right) - T_{r2}}{t_{n0}\beta_{12}} = \frac{t_{r0} - t_{n0} - T_{r2}}{t_{n0}\beta_{12}} - u_{rz}\frac{\left(t_{n0}\beta_{rp} + \tau_{1r}\right)}{t_{n0}\beta_{12}}. \tag{B.50}$$

We then substitute this equation into T_{21}, Eq. B.47, and solve for the recoil ion velocity, u_{rz}:

$$u_{rz} \simeq \frac{\left(T_{21} - t_{n0} + t_{p0}\right) t_{n0}\beta_{12} - \left(t_{r0} - t_{n0} - T_{r2}\right)\left(t_{n0}\beta_{12} + \tau_p\right)}{\left(t_{n0}\beta_{rp} - \tau_p\beta_{rp}\right) t_{n0}\beta_{12} - \left(t_{n0}\beta_{rp} + \tau_{1r}\right)\left(t_{n0}\beta_{12} + \tau_p\right)}. \tag{B.51}$$

Now that u_{rz} is known, we substitute it back into Eq. B.50 which yields

$$u'_{1z} \simeq \frac{t_{r0} - t_{n0} - T_{r2}}{t_{n0}\beta_{12}} - \frac{\left(T_{21} - t_{n0} + t_{p0}\right) t_{n0}\beta_{12} - \left(t_{r0} - t_{n0} - T_{r2}\right)\left(t_{n0}\beta_{12} + \tau_p\right)}{\left(t_{n0}\beta_{rp} - \tau_p\beta_{rp}\right) t_{n0}\beta_{12} - \left(t_{n0}\beta_{rp} + \tau_{1r}\right)\left(t_{n0}\beta_{12} + \tau_p\right)} \times \frac{\left(t_{n0}\beta_{rp} + \tau_{1r}\right)}{t_{n0}\beta_{12}}. \tag{B.52}$$

Both expressions for u_{rz} and u'_{1z} can probably be somewhat simplified.

Once u_{rz} is evaluated we can determine the longitudinal momentum transfer to the recoil ion, $P_\parallel$, and from it the reaction Q-value using the equations listed in sub-section B.3.

B.3 Reaction Q-Value

The reaction Q-value is related to the momentum transfer in the collision, or more specifically to the longitudinal momentum of the recoil ion, $P_\parallel$, as discussed in detail, *e.g.* by

Ullrich *et al.* [37]. Note that the relationship between the Q-value and the measured $P_\parallel$ of the recoil depends on the reaction mechanism.

In the previous sub-sections we detailed how the scaled longitudinal recoil-ion velocity, u_{rz}, can be evaluated from the measured TOF. Once u_{rz} is evaluated the longitudinal momentum transfer to the recoil ion can be determined to be

$$P_\parallel = M_r u_{rz} v_{0z} \tag{B.53}$$

(in a.u.). Recall that the Q-value is defined as the difference between the final and initial internal energies of the system, namely

$$Q \equiv E_f - E_i, \tag{B.54}$$

(note that exothermic reactions yield negative Q-values).
Most importantly, the Q-value can be determined experimentally from the longitudinal momentum of the recoil ion, $P_\parallel$, where the relationship between these two variables depends on the reaction mechanism (i.e. see Ref. [37]).

For electron capture, this relationship is

$$Q = v_{0z} P_\parallel + n_c \frac{1}{2} v_{0z}^2, \tag{B.55}$$

where n_c is the number of electrons captured.

For target ionization

$$Q = v_{0z} P_\parallel + \sum_{i=1}^{n_T} v_{0z} P_{ei\parallel} - \sum_{i=1}^{n_T} E_{if}\,, \tag{B.56}$$

where n_T is the number of electrons ionized from the target and E_{if} is the final energy of the ith electron emitted.

For electron loss (i.e. projectile ionization)

$$Q = v_{0z} P_\parallel - \sum_{i=1}^{n_p} E_{if}\,, \tag{B.57}$$

where n_p is the number of electrons ionized from the target (see Ref. [37]).

Appendix C

Variable Definitions

Table C.1: Definitions of the imaging equation variables.

m_1		mass of first beam fragment to hit detector
m_2		mass of second beam fragment to hit detector
M_p	$m_1 + m_2$	projectile mass
M_r		mass of recoil ion
β and β_{12}	m_1/m_2	mass ratio of beam fragments
β_{rp}	M_r/M_p	mass ratio of recoil ion and projectile
q		charge of beam fragment for cell setup
q_r		recoil charge
q_p		projectile charge
F		acceleration scaling factor
v_0 and v_{0z}	$\sqrt{\frac{2E_b}{m_1+m_2}}$	beam velocity
u_{jz}	v_{jz}/v_{0z}	scaled velocity for particle j
E_b		beam energy at the interaction point
a		acceleration in extraction field
V_s		the main spectrometer voltage
V_i		the spectrometer voltage at the interaction
V_f		the spectrometer voltage at the focus
V_1	$V_i - V_f$	first field region for jet setup
V_2	V_f-ground	second field region for jet setup
z_i		initial position of interaction
γ	$\frac{V_1}{V_2}\frac{l_2}{l_1}$	